Facultad de Ciencias. Sección de Física
Máster Universitario en Astrofísica

TRABAJO DE FIN DE MÁSTER

The formation of nearly bulgeless galaxies in cosmological simulations

---

Elena Arjona Gálvez
Tutor: **Dr. Claudio Dalla Vecchia**

Agradecimientos

A todas esas personas que me han dedicado parte de su tiempo durante todo este proceso. En especial a Isaac y Abraham por, a parte de tiempo, dedicarme toda la paciencia y cariño del mundo.

A mi *yayo*, tu fascinación por las constelaciones siempre permanecerá en mi memoria aunque ya no estés.

Contents

Resumen

El entendimiento de la morfología de las galaxias y su evolución con el paso del tiempo suponen, hoy en día, uno de los mayores campos de investigación en la astrofísica. Existen diversas teorías que explican esta evolución, la teoría más aceptada apoya un universo repleto de materia oscura fría (ΛCDM). El paradigma de esta teoría predice una evolución de las galaxias debida, en gran medida, a violentos procesos de fusión entre ellas en los cuales todo movimiento orbital existente se convierte en un proceso aleatorio de energía, lo que produce un cambio en la morfología de las galaxias.

Esta teoría de formación de galaxias ha sido notablemente existosa a lo largo de los años. Junto con el diagrama de Hubble (figura 1.1), el cual establece distintos tipos de galaxias dependiendo de la forma de estas, ha sido posible establecer una línea evolutiva en base a la morfología de las galaxias. Según este esquema, galaxias espirales, las cuales se caracterizan por un gran movimiento orbital, evolucionan a galaxias elípticas, cuyo movimiento es aleatorio, a través de violentas fusiones entre ellas. Sin embargo, la aparición de diversos estudios que afirman la existencia de una gran fracción de galaxias espirales con una componente pequeña o nula de bulbo sugiere un gran desafío bajo este modelo. Si todas las galaxias han sufrido fusiones entre ellas a lo largo de su historia evolutiva, reduciendo así la rotación global del sistema, la existencia de galaxias sin bulbo y, además, la gran fracción de ellas, pone en riesgo la veracidad de este canal evolutivo.

Bajo esta premisa, se crea el proyecto BEARD, el cual pretende analizar una muestra observada de 66 galaxias masivas espirales (galaxias con una masa mayor de 10^{10} masas solares) con una baja o nula presencia de bulbo. Este set de galaxias ha sido seleccionado del catálogo espestroscópico SDSS-DR13, el cual proporciona un marco excepcional para el estudio estadístico de las galaxias. Este *Trabajo de Fin de Máster* se incluye dentro de este proyecto, el cual pretende aportar un marco teórico a las observaciones a través de un análisis exhaustivo mediante simulaciones, donde es posible realizar un seguimiento en la historia evolutiva de las galaxias. Para esta labor se ha usado la mayor simulación cosmológica de EAGLE, la cual cuenta con un tamaño de $(100\ \mathrm{Mpc})^3$ y 2×1504^3 partículas de materia oscura y gas, donde se han seleccionado todas las galaxias espirales con una masa mayor de $M_* > 10^{10}$ masas solares. Una breve introducción al proyecto EAGLE y la simulación con la que trabajaremos se encuentra en la sección 3.1.

Al principio del proyecto se realizará una selección de todas las galaxias espirales de nuestra simulación que tengan masa mayor de $M_* > 10^{10} M_\odot$ (sección 3.2). Dicha selección se llevará a cabo usando parámetros cinemáticos tales como la fracción de estrellas en contra-rotación, k_{co}, el achatamiento, ε o la triaxialidad, T. Los límites establecidos para cada parámetro se han basado en los estudios realizados por Correa et al. (2017) y Thob et al. (2019).

Tras esto, se desarrollarán dos análisis cinemáticos en paralelo basados en estudios anteriores realizados por Zolotov et al. (2009) y Clauwens et al. (2018). Dichos estudios establecen dos tipos de técnicas de descomposición basadas en el momento angular de las estrellas pertenecientes a cada una de las galaxias. Para cada técnica, un cambio de referencia al sistema propio de cada galaxia es necesario, alineando la componente z del nuevo sistema de referencia con el momento angular global de su galaxia. Con esto, situamos la componente disco de cada una de las galaxias de nuestra muestra en el plano x-y, propio para cada una de ellas. Tras esto,

una descomposición en bulbo, halo y disco se realiza para cada uno de los métodos comentados anteriormente (Zolotov et al., 2009; Clauwens et al., 2018). Ambas descomposiciones cinemáticas se pueden encontrar ampliamente desarrolladas en la sección 3.3.1.

Por otra parte, con motivo de una comparación directa con las observaciones, también se realizará una clasificación fotométrica de la muestra de galaxias a través de un procedimiento análogo al criterio de selección usado por el proyecto BEARD. Dicha selección cataloga las galaxias con o sin bulbo dependiendo de su índice de concentración luminosa, siendo este el ratio entre el radio que encierra el 90% y el 50% del flujo petrosiano. Para esta clasificación, el proyecto BEARD se basa en el estudio realizado por (Graham & Driver, 2005), donde encuentra que las galaxias correspondientes a una concentración de luz menor de 2.5 corresponden a un índice Sérsic de n = 1.5. Esta selección pretende proporcionar galaxias masivas puramente espirales, es decir, sin bulbo. Un análisis más detallado del flujo petrosiano y el índice de concentración se puede encontrar en la sección 3.3.2.

Una vez realizadas las distintas clasificaciones, en el capítulo 4 se expone una comparación detallada entre las dos descomposiciones cinemáticas (sección 4.1.1) y se lleva a cabo un estudio de estas frente a la clasificación fotométrica. Tras esto, se establece la fracción de galaxias sin bulbo para cada una de las técnicas utilizadas (tabla 4.1). En la sección 4.2 se realiza, para cada uno de los métodos cinemáticos, un estudio de dependencia entre la mayor contribución de masa debido a una fusión en la historia de formación de las galaxias y su tamaño de la componente bulbo. Análogamente, se realiza este mismo estudio con respecto al índice de concentración de luz. Finalmente, aprovechando que el método de Zolotov et al. (2009) nos da información de todas las partículas pertenecientes a cada una de las componentes, se realiza un estudio de la edad media de las partículas del bulbo y su relación con el tamaño de este.

Debido a la resolución de nuestra simulación, las componentes con una escala resolutiva menor de aproximadamente 3 kpc, como lo son los bulbos pequeños, están próximos al limite de resolución, por lo que los resultados extraídos de los análisis se tienen que interpretar con cuidado. En el capítulo 5 se encuentran las correspondientes conclusiones ligadas a estos resultados, así como una enumeración de los diferentes tipos de objetivos futuros que este trabajo nos ha ido planteando.

Chapter 1

Introduction

1.1 Galaxy formation and morphology

The Hubble tuning fork diagram (Hubble, 1936) has provided for years the most popular way to galaxy classification, based on their morphologies. Nevertheless, this scheme has been revised in the recent years in order to accommodate photometric and kinematic properties of galaxies (Cappellari et al., 2011; Kormendy & Bender, 2012). The relative size of the bulge compared with the galaxy has been one of the primary features to classify galaxies in the different Hubble types (figure 1.1). Spiral galaxies are known to have a central bulge, similar to an elliptical galaxy, and two types of disks: a stellar disk like S0 type and a disk of gas, stars and other interstellar matter that forms the spiral pattern. However, the definition of bulge is not straightforward, and is still a challenge for contemporary astrophysics.

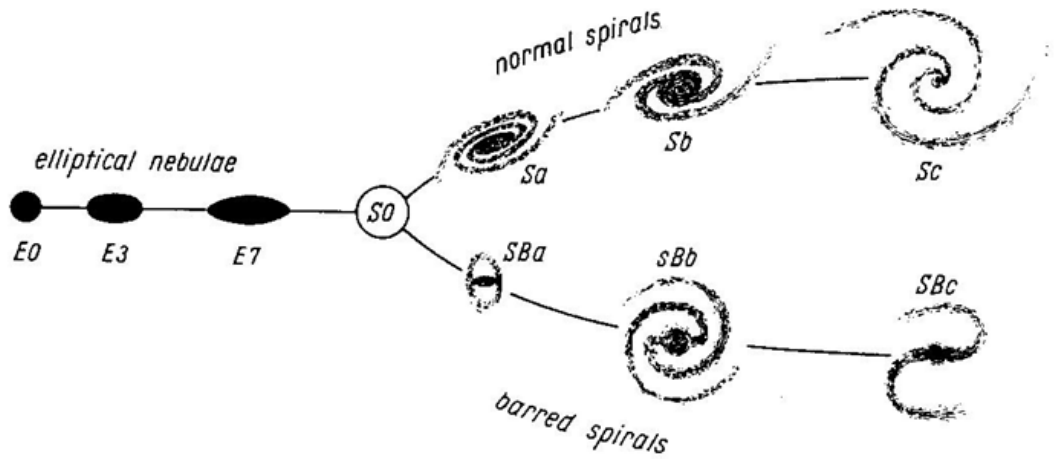

Figure 1.1: The Hubble tunning fork diagram

Galaxy morphology is closely linked to other galaxy properties. More massive galaxies are generally less disky and, at fixed mass, star-forming galaxies tend to be disk-dominated, while quiescent galaxies are typically bulge-dominated (Gadotti, 2009; Bluck et al., 2014; Whitaker et al., 2015). Above $10^{10} M_{\odot}$ the stellar mass at low redshift is roughly equally divided between elliptical, classical bulges and disk galaxies (Gadotti, 2009). There is good evidence that high-redshift galaxies are built from these same morphological components with a qualitatively similar dependency on star formation and mass (van Dokkum et al., 2014; Tacchella et al., 2015).

One can decompose most galaxies into components that are either rotation or dispersion supported. This decomposition is motivated by the fact that classical bulges are very similar to elliptical galaxies, suggesting a similar formation mechanism. Galactic bulges are frequently classified as classical or pseudo-bulges (Andredakis & Sanders, 1994; Wyse et al., 1997). Classical bulges are known to have spheroidal symmetry, older stellar populations and supported by velocity dispersion. Whereas pseudo-bulges are rotationally dominated and with diverse possible shapes like "disky", boxy/"peanut" or nuclear bars. Milky Way-like galaxies exhibit a large range of bulge properties and sizes, from prominent (e.g., M31), to almost non-existing bulges (e.g., M101). The diversity in the properties of these galaxies reveals the existence of different formation paths in the context of the hierarchical galaxy formation paradigm (White & Rees, 1978), which are not fully understood.

There are many possible scenarios for bulge formation. Pseudobulges can form through secular processes (Kormendy & Kennicutt, 2004) such as bar formation, followed by a buckling instability that transforms the bar into a peanut shaped pseudobulge (Raha et al., 1991; Pohlen et al., 2003; Guedes et al., 2013). Classical bulges can form from diverse processes such as the collapse of primordial gas clouds (Eggen et al., 1962), disk instabilities (Lucia et al., 2011), clump migration to the galaxy center in violently unstable gas rich disks at high redshift (Noguchi, 1999; Bournaud et al., 2007, 2011; Perez et al., 2013; Ceverino et al., 2015), gas funneling to the center in marginally unstable disks at high redshift (Krumholz et al., 2018), misaligned accretion (Sales et al., 2012; Aumer et al., 2013) and mergers (Aguerri et al., 2001; Hopkins et al., 2010; Bournaud et al., 2011; Lucia et al., 2011; Aumer et al., 2013; Ceverino et al., 2015). The similarities between elliptical galaxies and classical bulges place the merger hypothesis as the most probable process to bulge formation.

Mergers can influence bulge growth and overall morphological changes in diverse ways. Hernquist (1989) finds that tidal effects during mergers may induce instabilities that can funnel a large amount of gas into the central region of a galaxy, thereby inducing a starburst which creates a spheroidal component. In order to prevent the formation of too massive bulges, stellar feedback is invoked to remove low angular momentum gas, also during merger induced starburst (Governato et al., 2009, 2010; Brook et al., 2011; Zjupa & Springel, 2017). This may not be sufficient and AGN feedback might be needed for a

further suppression. Disks can be destroyed by major merger, but they also can regrow afterwards due to major merger remnants, which can provide enough gas available for star formation. (Governato et al., 2009; Lucia et al., 2011; Sparre & Springel, 2017).

1.2 Bulgeless galaxies

The current theory for structure formation in the Universe (including galaxies, galaxy clusters, and large-scale structures) predicts hierarchical clustering in a Λ Cold Dark Matter (ΛCDM) framework. This theory has been very successful at describing the evolution of Mpc-size structures. However, at subgalactic scales (kpc-size), the nonlinear processes involving baryonic physics (such as gas heating and cooling, star formation and feedback) are thought to play a substantial role in shaping the internal galaxy structure and the overall star formation history of the universe. A fundamental problem of ΛCDM hydrodynamical simulations is to reproduce the observed fraction of massive bulgeless galaxies (i.e., galaxies with small bulges or pure-disk ones) in the local Universe (Kormendy et al., 2010; Shen et al., 2010; Fisher & Drory, 2011). Since galactic disks are fragile systems that get easily destroyed or perturbed by mergers, massive galaxies in simulations generally end up beeing either elliptical galaxies or disk galaxies with massive central bulges. If massive, bulgeless galaxies ($M_* > M_{\odot}^{10.5}$) are proved not to have undergone any past or recent mergers, then either the theory of ΛCDM or its baryonic implementations should be revisited.

Over the last decade, cosmological hydrodynamical simulations that use feedback due to supernovae or active galactic nuclei, and continuous accretion of cold gas via cosmic filaments, achieved a major step forward by creating bulgeless, dwarf disk galaxies for the first time (Governato et al., 2010). However, the same star formation and feedback models that lead to bulgeless dwarf disk generally yield to overly massive stellar bulges for Milky Way-like galaxies ($M_* > M_{\odot}^{10.5}$) (Christensen et al., 2014). The simple solution of increasing the feedback at larger galaxy masses has reduced the size of bulges in Milky Way-like galaxies (Aumer et al., 2013) with the counter effect that galaxies are too large compared to observed galaxies (Aumer et al., 2014). Therefore, massive bulgeless galaxies are still a challenge for ΛCDM models.

The first comprehensive search for disk-dominated and bulgeless galaxies was initiated by (Karachentsev, 1989). He classified edge-on disk galaxies, where bulges can be easily detected and the vertical structure can be studied. This work resulted in the Flat Galaxy Catalog (Karachentsev et al., 1993), the Revised Flat Galaxy Catalog (Karachentsev, 1999) and the 2MASS-selected Flat Galaxy Catalog (Mitronova et al., 2004). More recently, (Kautsch, 2009) used a complete sample of edge-on galaxies from the Sloan Digital Sky Survey (SDSS), finding that 16% of disk galaxies are bulgeless. However, studies based on edge-on samples present issues related to the fact that other galaxy properties cannot be measured, such as the presence of obscured and compact bulges, due to dust extinction. Therefore, a systematic search for bulgeless galaxies in less inclined

galaxies is a must to solve the conundrum of their hierarchical formation. Previous studies of moderately-inclined bulgeless galaxies used either detailed analysis of large samples (Böker et al., 2002; Kormendy et al., 2010) or simple photometric analysis of large samples (Barazza et al., 2008; Méndez-Abreu et al., 2017), thus providing an uncertain fraction of bulgeless galaxies in the nearby Universe spanning from 20% (Barazza et al., 2008) to 74% (Kormendy et al., 2010).

1.2.1 The BEARD project

A definitive solution to the problem of bulgeless galaxies in a hierarchical ΛCDM Universe requires a detailed analysis of the merging history of a statistically significant sample of bulgeless galaxies. To this aim, the BEARD (**B**ulgeless **E**volution **A**nd the **R**ise of **D**isks) project was started.

The plan of the BEARD project is to observe a volume limited sample of 66 massive ($> 10^{10} M_{\odot}$), bulgeless galaxies in the nearby Universe (< 40 Mpc) using high spectral resolution spectroscopy to classify their central bulge/structure, deep broad-band photometry to characterize their outskirts looking for signs of mergers and narrow-band photometry in order to measure the more recent star formation. Their sample of bulgeless galaxies has been selected from the SDSS-DR13 spectroscopic catalogue, which provides a unique framework for statistical galaxy studies.

For a good photometric definition of the bulge region and limiting the effects of dust lanes, they impose an inclination of i < 60 degrees to their sample. In order to get a sample of massive bulgeless galaxies, they choose only galaxies with light concentration index C = R90/R50 < 2.5 (Graham & Driver, 2005) and a Pretrosian radius, r_p larger than 10 arcsec (both parameters will be defined in section 3.3.2). The results of this project will provide the necessary observational constraints to demonstrate the success or failure of the hierarchical ΛCDM scenario at galactic scales.

Cosmological simulations are the ideal place to test the physics of bulge formation, because the complex processes of mergers, stellar feedback and gas inflow and outflow can be self-consistently modeled. Until recently, however, it has been very difficult to specifically study bulge formation due to bulges being generally in the same size scale as the force resolution. Convergence in the density profile is only achieved when enough particles are enclosed that the time scale for collisional relaxation of the particles is larger than the age of the Universe (Power et al., 2003). In practise, this means that densities usually converge at about 5 times the force softening length (Navarro et al., 2010). In addition, hydrodynamical simulations, historically, have produced too massive and dense central stellar concentration on galaxies at high redshift, akin to bulges, which introduce a significant bias in the bulge study (Brooks & Christensen, 2016). This problem is known as the overcooling problem.

The goal of this work is to provide a theoretical framework for the BEARD observational results using state-of-the-art cosmological simulations. To do this, we will use the EAGLE simulation (Crain et al., 2015; Schaye et al., 2015), one of the largest cosmological hydrodynamical simulations to this date. Our first step will be to select a sample of galaxies at z = 0 with the same constraint used in the BEARD project. The merger history will be followed back in time to compare with the observations. Although EAGLE does not have enough resolution to confidently reproduce the smallest observed bulges, it has overcome the major hurdle: the overcooling problem.

Chapter 2

Objectives

In the present work we aim to accomplish the following objectives:

1. To identify a sample of simulated disk galaxies with masses within the observed range in high resolution simulations using kinematic and observational techniques. In order to do this we are going to use the EAGLE simulations.

2. To decompose our sample of galaxies into kinematics and observational components and measure the size of their bulge using different techniques.

3. To compare two state-of-the-art kinematics techniques (Zolotov et al., 2009; Clauwens et al., 2018), used to decompose the galaxies, and see the analogies and differences between them.

4. To compare both kinematic methods (Zolotov et al., 2009; Clauwens et al., 2018) with the observational method used by the BEARD project to follow possible analogies with observational samples.

5. To reconstruct the formation history of our sample galaxies, in order to understand the frequency of minor and major mergers in their evolution, and search for a correlation between the size of the bulge and their merger history for each decomposing method used.

The first and second objectives are partially discussed in the next chapter, namely in sections 3.2 and 3.3, respectively. More importantly, their accomplishment is the base for the last objectives and will be described in chapter 4.

Chapter 3

Methodology

3.1 The EAGLE project

To study the assembly and evolution of galaxies, rigorous techniques need to be developed to test the different theories. The physical and astrophysical phenomena behind galaxy evolution are highly non-linear, making any analytical description hard to reach. For this reason, the massive use of numerical simulations has considerably improved our understanding of cosmological events.

One of the most important tools that can be used to model galaxies and, simultaneously, the intergalactic medium (IGM), is cosmological hydrodynamical simulations. They allow us to achieve a better understanding of the feedback cycles and fuelling of a large variety of galaxies. If the similarities between observations and hydrodynamical simulations of galaxy formation are sufficiently strong, the latest can be used to calculate cosmological and physical parameters that we could not measure only with observations, e.g., the thermal evolution of the intergalactic medium (Croft et al., 1998; Schaye et al., 2000; Viel et al., 2004; McDonald et al., 2005).

With this objective in mind, the Virgo Consortium has developed the "**E**volution and **A**sembly of **G**a**L**axies and their **E**nviorments" (hereafter EAGLE) project for cosmological hydrodynamical simulations (Crain et al., 2015; Schaye et al., 2015). The EAGLE project consists of a suite of cosmological hydrodynamical simulations in which the main models were run in cubic, periodic volumes with length of 12, 25, 50, and 100 comoving Mpc (cMpc), designed to reproduce the evolution and formation of galaxies, i.e., to track the evolution in time from a redshift 127 to the present day of baryonic and non-baryonic matter. This is possible thanks to calibrations within a limited subset of observations of $z = 0$ galaxies, such as the stellar mass function of galaxies, their sizes and the correlation between stellar and black hole mass.

All simulations use a modified version of the GADGET-3 Tree-SPH, N-body Tree-PM smoothed particle hydrodynamic code based on the GADGET-2 code (Springel, 2005), that includes the implementation of a large number of subgrid modules that supply physical processes with a limited resolution scale such as stellar evolution, star formation, metal enrichment, feedback from stars, the feedback generated by merging and accretion of supermassive black holes, etc. All these processes are described in Schaye et al. (2015) and references there in.

The EAGLE simulations adopt a flat ΛCMD cosmology with the parameters listed below (table 3.1), determined by the Planck Collaboration (Ade et al., 2014). The initial conditions have been generated using the second-order Lagrangian perturbation theory (Jenkins, 2010).

Ω_Λ	Ω_m	Ω_b	σ_8
0.693	0.307	0.04825	0.8288
n_s	Y	H_0 [km s^{-1} Mpc^{-1}]	
0.9611	0.248	67.77	

Table 3.1: Cosmological parameters used by the EAGLE simulations.

In this work we use RefL0100N1504, a hydrodynamical simulation with a force resolution of 0.7 pkpc which we refer to as intermediate resolution. This is the largest EAGLE simulation, with a comoving box size of 100 Mpc and 1504^3 dark matter particles (being, at the initial time, the same number of baryonic particles). In addition, this simulation has a mass resolution of 1.81×10^6 M$_\odot$ for gas particles and 9.70×10^7 M$_\odot$ for dark matter particles (McAlpine et al., 2016).

The simulation relies on subgrid models for unresolved processes at small scales and low temperatures in the interstellar medium, meaning that, by design, the simulation does not produce cold thin disks. The minimum resolved scale is about 1 kpc, which means that the simulation is best suited to study bulges at the high-mass end of the mass-size relation and the transformation of disk galaxies into elliptical galaxies. However, Clauwens et al. (2018) show that, although EAGLE lacks the resolution to confidently reproduce the smallest observed bulges, it has overcome the overcooling problem and does well in this regard, and suggest a good convergence of the results in their analysis for galaxies with a stellar mass larger than 10^9 M$_\odot$.

3.2 Sample selection

Several diagnostic quantities are frequently used to characterise the kinematic properties of simulated galaxies and are, in general, condensed into a single indicator such as a bulge-to-total ratio (B/T), disk-to-total ratio (D/T) or a morpho-kinematic parameter, κ_{rot} (Scannapieco et al., 2010; Sales et al., 2010, 2012; Zavala et al., 2016; Bottrell et al., 2017; Correa et al., 2017).

Correa et al. (2017) pointed out that spiral galaxies can be found through their amount of co-rotational velocity and defined the rotational kinetic energy parameter, κ_{co}, as the fraction of a particle's total kinetic energy, K, that is invested in co-rotation, K_{co}^{rot}:

$$\kappa_{co} = \frac{K_{co}^{rot}}{K} = \frac{1}{K} \sum_{i, L_{z,i}>0} \frac{1}{2} m_i \left(L_{z,i}/m_i R_i\right)^2 \tag{3.1}$$

where the sum is over all co-rotation ($L_{z,i} > 0$) stellar particles within 25 pkpc. R_i is the 2-dimensional radius in the plane normal to the rotation axis and m_i is the mass of each stellar particle. The total kinetic energy in the center of mass frame is $K = \sum_i \frac{1}{2} m_i v_i^2$, again summing over all stellar particles within 25 pkpc.

Correa et al. (2017) used this diagnostic to characterise the kinematics of EAGLE galaxies, and found that, splitting the galaxies through a threshold in κ_{co}, provides a way of separating disky, star-forming galaxies ($\kappa_{co} > 0.4$) from spheroidal, passive galaxies ($\kappa_{co} < 0.4$).

One can also obtain a quantitative description of the galaxies structure by modelling the spatial distribution of their stars. Thob et al. (2019) used an ellipsoid model to describe the stellar distribution of EAGLE galaxies, characterised by the flattening, ε, and triaxiallity, T,parameters. These parameters are defined as:

$$\varepsilon = 1 - \frac{c}{a}, \quad \text{and} \quad T = \frac{a^2 - b^2}{a^2 - c^2} \tag{3.2}$$

where a, b and c are the moduli of the major, intermediate and minor axes, respectively. For spherical haloes, $\varepsilon = 0$ and T is undefined, whilst low and high values of T correspond to oblate and prolate ellipsoids, respectively. Thob et al. (2019) used a threshold of $\varepsilon > 0.5$ and $T < 0.3$ to define disky galaxies.

In order to reproduce the galaxy selection of the BEARD observations, we have extracted from EAGLE all the Milky Way-like galaxies within the respective simulation. To do this, we first choose all the central galaxies with a stellar mass larger than 10^{10} $M_\odot$. Then, we used several kinematic morphology indicator to select all the disk galaxies, such as a stellar counter-rotating kinetic energy fraction, κ_{co}, larger than 0.4 (Correa et al., 2017), a flattened, ε, larger than 0.5 and a triaxiallity, T, lower than 0.3 (Thob et al., 2019). This selection criteria leave us with a sample of 894 massive disk galaxies.

3.3 Bulge detection

The aim of this work is the study of the formation of bulgeless galaxies. In an attempt to do this, two different kinematics analysis of the stellar particles in each galaxy were done to decompose them into disk, bulge and halo kinematic components.

Additionally, in order to follow an analogue procedure with the observations, we measured the concentration index for each galaxy, $C = R90/R50$ (as we will see in subsection 3.3.2). Graham & Driver (2005) show that a light concentration $C = 2.5$ is equivalent to a Sérsic index $n = 1.5$ and, therefore, all the sample with a light concentration smaller than 2.5 is dominated by late-type disk galaxies.

For the purpose of analysing each individual galaxy, it is indispensable to change the global system of reference of the simulation to a proper galaxy reference system. To do this, we compute the center of mass of all the stellar particles within 25 kpc from the center of potential, and set that as the origin. Then, we align the $\hat{z}$-axis with the total stellar angular momentum in the galaxy.

To this end, we first need to shift the system of reference from the global system to the individual galaxy systems. For this purpose, we use the equation:

$$\vec{r}_{galaxy} = \vec{r}_{EAGLE} - C\vec{M}_{galaxy} \tag{3.3}$$

where $\vec{r}_{EAGLE}$ are the coordinates of all the particles in the global coordinate system and $C\vec{M}_{galaxy}$ is, for each galaxy, the center of mass of the galaxy system of reference.

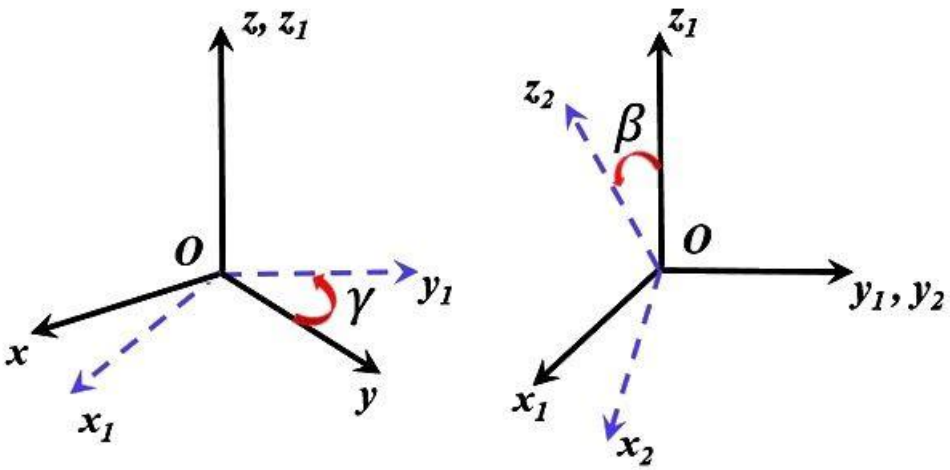

Figure 3.1: Rotation from the initial orientation to the angular moment vector of the galaxy.

Once we have one system for each galaxy, the idea is to align the global angular momentum of the galaxy with the $\hat{z}$-axis to place the disk of the galaxy in the $\hat{x} - \hat{y}$ plane. In figure 3.1 we see the two different rotations that we need to take into account when placing the disk on the required plane. The γ and β angles are defined by equations 3.4, the (x, y, z) coordinates are the initial coordinates before any rotation and (x_2, y_2, z_2) defines the coordinates after all the changes.

$$\beta = \arccos s_z; \quad \gamma = \arctan\left(\frac{s_y}{s_x}\right) \tag{3.4}$$

where (s_x, s_y, s_z) is the normalize global angular momentum of the galaxy.

The first rotation is made around the $\hat{z}$-axis a γ angle. Then, a second rotation around the $\hat{y}$-axis a β angle is necessary to orient the plane perpendicular to the global angular momentum. Both rotation matrices are represented in equation 3.5.

$$R(\gamma) = \begin{pmatrix} \cos\gamma & \sin\gamma & 0 \\ -\sin\gamma & \cos\gamma & 0 \\ 0 & 0 & 1 \end{pmatrix}; \quad R(\beta) = \begin{pmatrix} \cos\beta & 0 & -\sin\beta \\ 0 & 1 & 0 \\ \sin\beta & 0 & \cos\beta \end{pmatrix} \tag{3.5}$$

The final coordinates with the reference system of the galaxy oriented with the global angular momentum are represented by the following equation:

$$\begin{pmatrix} x_2 \\ y_2 \\ z_2 \end{pmatrix} = R(\beta, \gamma) \begin{pmatrix} x \\ y \\ z \end{pmatrix} \tag{3.6}$$

$$R(\beta, \gamma) = R(\beta)R(\gamma) = \begin{pmatrix} \cos\beta\cos\gamma & \cos\beta\sin\gamma & -\sin\beta \\ -\sin\gamma & \cos\gamma & 0 \\ \sin\beta\cos\gamma & \sin\beta\sin\gamma & \cos\beta \end{pmatrix} \tag{3.7}$$

where the rotation matrix, $R(\beta, \gamma)$, is the composition of the two rotations mentioned above, $R(\gamma)$ and $R(\beta)$, and it is defined in equation 3.7.

Once the reference system has been well defined, we can perform the proper analysis to estimate the fraction of stellar particles belonging to the bulge of each galaxy. In the following sections, we will describe the various methods applied in this work.

3.3.1 Kinematic classification

A kinematic analysis of the stellar particles in each galaxy was done to decompose them into disk and classical bulge. Once we have all the galaxies aligned with their total stellar angular momentum, we measure the specific angular momentum of individual stellar particles $\vec{j}$, defined by:

$$\vec{j} = \begin{vmatrix} \hat{x} & \hat{y} & \hat{z} \\ x & y & z \\ v_x & v_y & v_z \end{vmatrix} = (yv_z - zv_y)\hat{x} + (zv_x - xv_z)\hat{y} + (xv_y - v_x y)\hat{z} \tag{3.8}$$

where, (x, y, z) are the coordinates of each stellar particle in the galaxy system of reference, and (v_x, v_y, v_z) are their respective velocities.

We now have all the ingredients to develop a proper kinematic decomposition of the galaxies. In this work, each simulated galaxy has been decomposed into a disk, bulge and halo kinematic components. We used two different ways to accomplish this. The first decomposition is based on Zolotov et al. (2009) while the other is the technique used in the EAGLE project to measure the stellar particles belonging to the disk and bulge+halo (Crain et al., 2010; McCarthy et al., 2012). Due to EAGLE not making a distinction between halo and bulge particles, we are going to split these two components following the same procedure as in Clauwens et al. (2018). The aim of this is to evaluate the analogies or discrepancies of choosing one method or the other.

For the decomposition based on Zolotov et al. (2009), we use the angular momentum of each star in the $\hat{x} - \hat{y}$ plane, j_z, obtained through equation 3.8. Also, we calculate the specific angular momentum of the co-rotating circular orbit with similar orbital energy, j_{circ}. To do so, we calculate, for each stellar particle, the enclosed mass of all the particles inside its orbit around the center of stellar mass. For a stellar particle i, $j_{i,circ}$ is obtained as:

$$j_{c,i} = r_i v_{c,i} = \sqrt{GM(r < r_i) r_i} \tag{3.9}$$

where $j_{c,i}$ is the circular moment of a stellar particle i, r_i is the radius of this the stellar particle, $M(r < r_i)$ the enclosed mass of all the particles within r_i and G is the gravitational constant.

Within this framework, a star with a circular orbit in the plane of the disk will have $j_z/j_{circ} \sim 1$. Stars with $j_z/j_{circ} \geq 0.8$ are selected as disk stars. The cut is chosen because it is equivalent to an eccentricity cut of $e \leq 0.2$, which matches the eccentricities observed in the Milky Way's disk (Nordström et al., 2004). Then, Zolotov et al. (2009) follow a classic definition of the bulge and define a spheroid made by stellar particles of the halo and bulge. The spheroid of each galaxy is defined using a cut in j_z/j_{circ} such that the spheroidal population does not exhibit a net rotation. Figure 3.2 shows, for one galaxy, the cut of j_z/j_{circ} where a null net rotation is found, i.e. all the stellar particles that have j_z/j_{circ} less than $(j_z/j_{circ})_{cut}$ and that, therefore, belong to the spheroidal component.

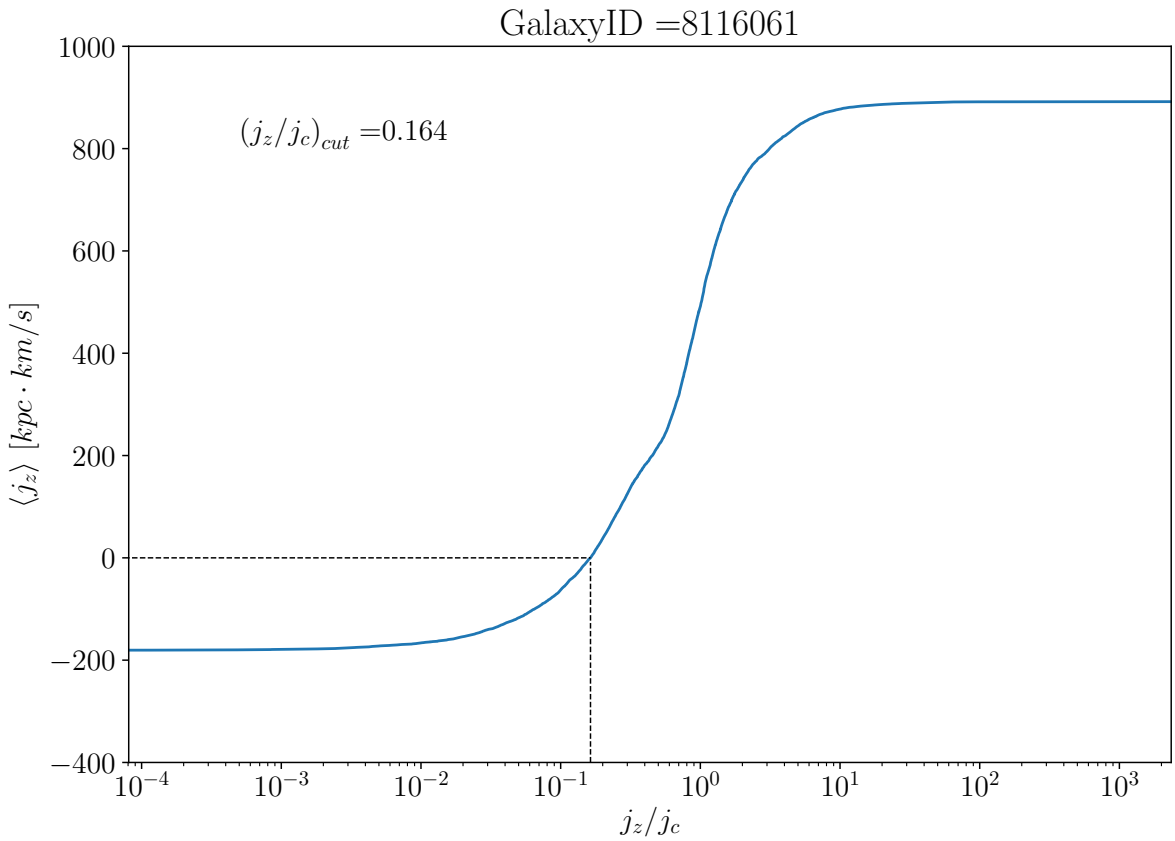

Figure 3.2: Net rotation of a spherical component with stellar particles that have a specific rotation smaller than j_z/j_c for the galaxy 8116061. The dashed lines show the cuts where the spheroid with null net rotation is located.

So far, we have the spheroid with a zero net rotation and we need to isolate the bulge particle from the halo. To do this, the break in the mass density profile is used. Stars which are tightly bound to the galaxy, those whose total energy is low, are classified as bulge stars, while all other stars are identified as stars of the halo. Stellar particles belonging to the bulge are placed within the break of the mass profile while halo stars are located outside the break. Figure 3.3 shows an example profile. The density profile has been fitted with a double power law that follows the equation:

$$\rho(r) = \frac{C}{r^{\gamma}\left(1 + r^{1/\alpha}\right)^{(\beta-\gamma)\alpha}} \tag{3.10}$$

where r is the radius of the stellar particles belonging to the spherical component and the parameters C, α, β and γ are calculated for each galaxy in order to dig up the accurate fit. At small radii, $\rho \sim r^{-\gamma}$, while at large radii $\rho \sim r^{-\beta}$. The parameter α determines the 'sharpness' of the break.

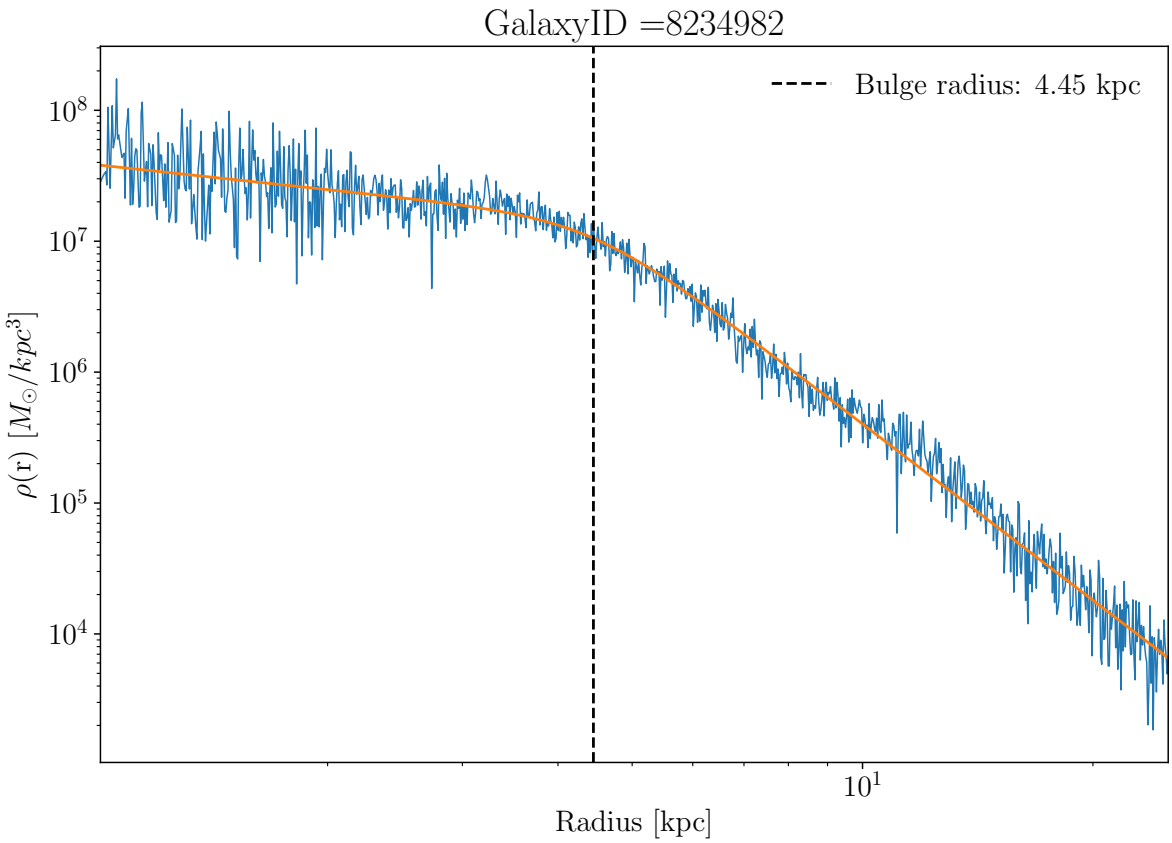

Figure 3.3: Mass density profile of the spheroidal component for the galaxy 8234982. The vertical line shows the radius where the break of mass occurs.

On the other hand, for the classification based on Clauwens et al. (2018) we follow a similar analysis than that made in EAGLE. In this method we normalise the angular momentum of each stellar particle in the $\hat{z}$-direction, j_z, by the total angular momentum of the given particle, $|\vec{j}|$. The resulting variable, $j_z/|\vec{j}|$, denotes the amount of co-rotation for each stellar particle within 25 kpc from the center of the galaxy. Stars that co-rotate with the stellar disk have $j_z/|\vec{j}| = 1$, stars that counter-rotate have $j_z/|\vec{j}| = -1$, and stars with random directions of angular momentum are distributed uniformly between 1 and -1. With this variable, we look again for a spheroidal component with mass S that is twice the mass of counter-rotation stars, i.e, twice the mass of stars with $j_z/|\vec{j}| < 0$ (equation 3.11). Note that the spheroidal component includes both bulge and halo and, unlike Zolotov et al. (2009) method, there is no distinction based on radius.

$$\frac{S}{T} = 2\frac{1}{M_*}\sum_{i,\frac{j_{z,i}}{|\vec{j}_i|}<0} m_i \tag{3.11}$$

where the sum is over all counter-rotating stellar particles within 25 pkpc, m_i is the mass of each stellar particle, and $j_z/|\vec{j}|$ is the ratio between its angular momentum projected

along the rotation axis and its total angular momentum. Thus, the ratio S/T is used to quantify the stellar morphology of each galaxy, being T the total stellar mass.

To split this spheroidal component into stellar bulge and stellar halo, Clauwens et al. (2018) use the S/T ratio (equation 3.11) for stars within 5 pkpc of the galaxy's center, catalogued as B/T, and for stars outside 5 pkpc, which are catalogued as halo particles and will be labeled as H/T.

3.3.2 Photometric classification

Now that we have the kinematic analysis of the different components of each galaxy, a photometric analysis is needed to make a proper comparison with the observations. In order to do this, we have to employ the Petrosian magnitudes. The definition of these magnitudes was introduced with the aim of measuring galaxy evolution. It gained additional popularity due to its potential to determine cosmological parameters (Djorgovski & Spinrad, 1981; Sandage & Perelmuter, 1990). Nowadays, it is often used as a tool for defining aperture sizes from which to measure galaxy luminosities.

Blanton et al. (2001) defined the "Petrosian ratio", $\mathfrak{R}_P$, at the radius r from the center of an object as the ratio of the local surface brightness averaged over an annulus at r to the mean surface brightness within r[1]:

$$\mathfrak{R}_P(r) = \frac{\int_{\alpha_{lo}r}^{\alpha_{hi}r} dr' 2\pi r' I(r') / [\pi \left(\alpha_{hi}^2 - \alpha_{lo}^2\right) r^2]}{\int_0^r dr' \pi r' I(r') / \left(\pi r^2\right)} \tag{3.12}$$

where $I(r)$ is the azimuthally averaged surface brightness profile and $\alpha_{lo} < 1$, $\alpha_{hi} > 1$ define the annulus. The SDSS has adopted α_{lo} and α_{hi} as 0.8 and 1.25, respectively.

The Petrosian radius r_P is defined as the radius at which $\mathfrak{R}_P(r_P)$ equals some specified value $\mathfrak{R}_{P,lim}$. The Petrosian flux in any band is then defined as the flux within a certain number N_P of Petrosian radii:

$$F_P = \int_0^{N_P r_P} 2\pi r' dr' I(r') \tag{3.13}$$

SDSS has selected $\mathfrak{R}_{P,lim} = 0.2$ and $N_P = 2$. Blanton et al. (2001) show how the aperture $2r_p$ is large enough to contain nearly all the light for a typical galaxy profile.

Given the Petrosian flux, one can find the radius R50 and R90, containing 50% and 90% of the Petrosian flux, respectiely. Blanton et al. (2001) defined the "concentration index" of galaxies as $C = R90/R50$. With this definition, Graham & Driver (2005) expose

[1]Throughout this section, for simplicity reasons, we will refer to r as the radius projected in the $\hat{x} - \hat{y}$ plane. We will have to take into account that this notation differs in the other sections.

that a concentration index of $C = 2.5$ is equivalent to a Sérsic index of $n = 1.5$. The BEARD project uses this affirmation to search for galaxies with a concentration index smaller than 2.5 and a Petrosian radius larger than 10 arcsec, obtaining in this way a sample dominated by late-type disk galaxies.

Therefore, with the aim to perform a similar analysis as that used in the observations, we calculate the concentration index for each galaxy. For this purpose, we extract from the EAGLE database the r band absolute magnitude in the AB system for all the stars within our galaxy sample. From these magnitudes, we can calculate the flux with the following equation (3.14):

$$m_{AB} = -2.5 \log f_\nu - 48.60 \longrightarrow f_\nu = 10^{-(m_{AB}+48.60)/2.5} \tag{3.14}$$

with f_ν in $\mathrm{erg} \cdot \mathrm{s}^{-1}\mathrm{cm}^{-2}\mathrm{Hz}^{-1}$.

Once we have the flux, we can obtain the azimuthally averaged brightness profile, $I(r)$. To do this, we bin the projected radius and measure the total flux inside each bin. Thus, the azimuthally averaged brightness profile can be obtained as:

$$I(r) = \frac{\sum_{r_i} f_{\nu,i}}{2\pi r \mathrm{d}r} \tag{3.15}$$

where the sum of f_ν is within the annule in for each bin, r is the average projected radius in this annule and $\mathrm{d}r$ is the width of the annule.

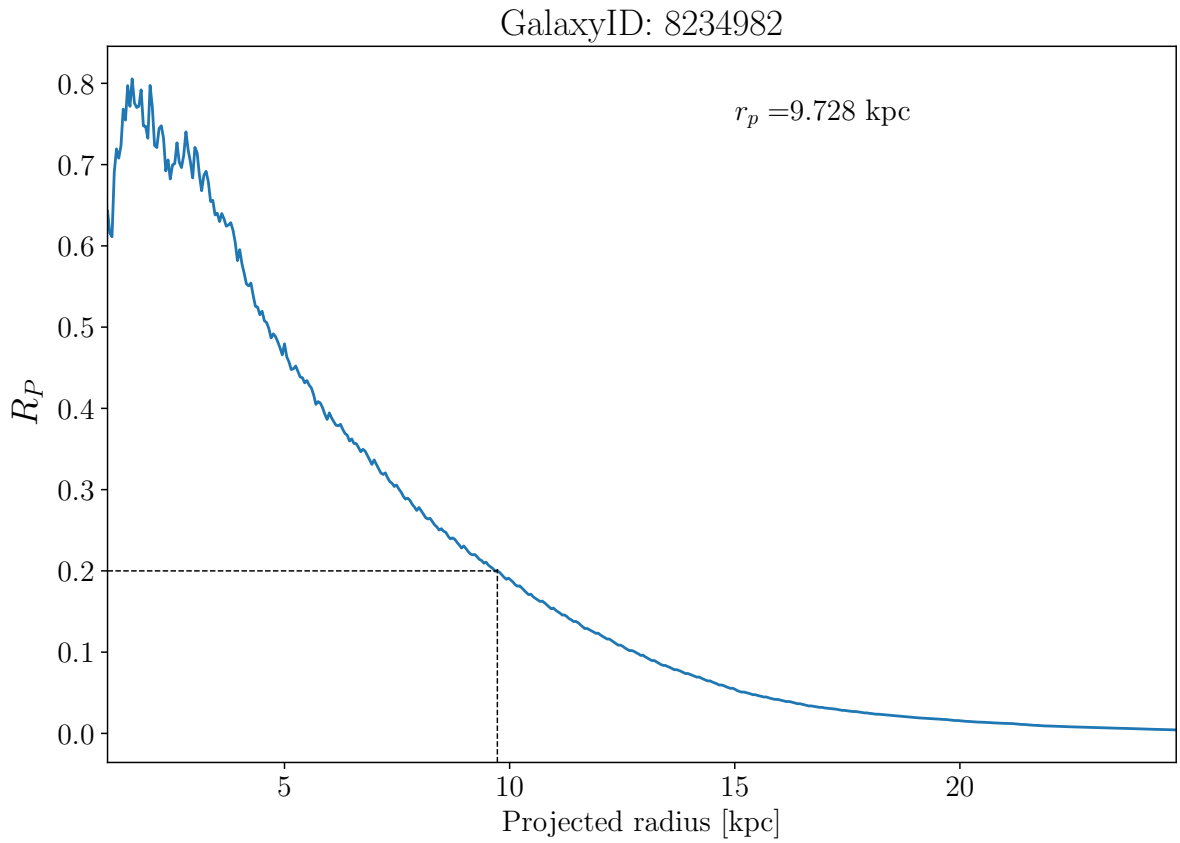

Figure 3.4: Petrosian ratio, eq 3.12, along the projected radius of the galaxy 8234982. The dashed lines indicate the value of the projected radius for a Petrosian ratio equal to 0.2, i.e, the Petrosian radius.

Now that we have $I(r)$, we can calculate the concentration index. First, it is necessary to find the Petrosian radius. To do this, we use equation 3.12 and measure the radius where this ratio has a value of 0.2. We calculate the integral of equation 3.12 for each projected radius, r, using the SDSS values of $\alpha_{lo} = 0.8$ and $\alpha_{hi} = 1.25$. Fig 3.4 shows the Petrosian ratio 3.12 along the projected radius for a specific galaxy. The r_P value is that with the closest value to $\mathfrak{R}_P(r_P) = 0.2$ that we find for each galaxy.

Once the Petrosian radii have been obtained, the concentration index can be trivially computed. We measure the total flux inside $2r_P$ and then take the radius that contains the 50% and 90% of this total flux. Finally, the concentration index will be the ratio between R90/R50. In figure 3.5 we show the value of the ratio between the Petrosian flux and the total Petrosian flux along the projected radius for a specific galaxy.

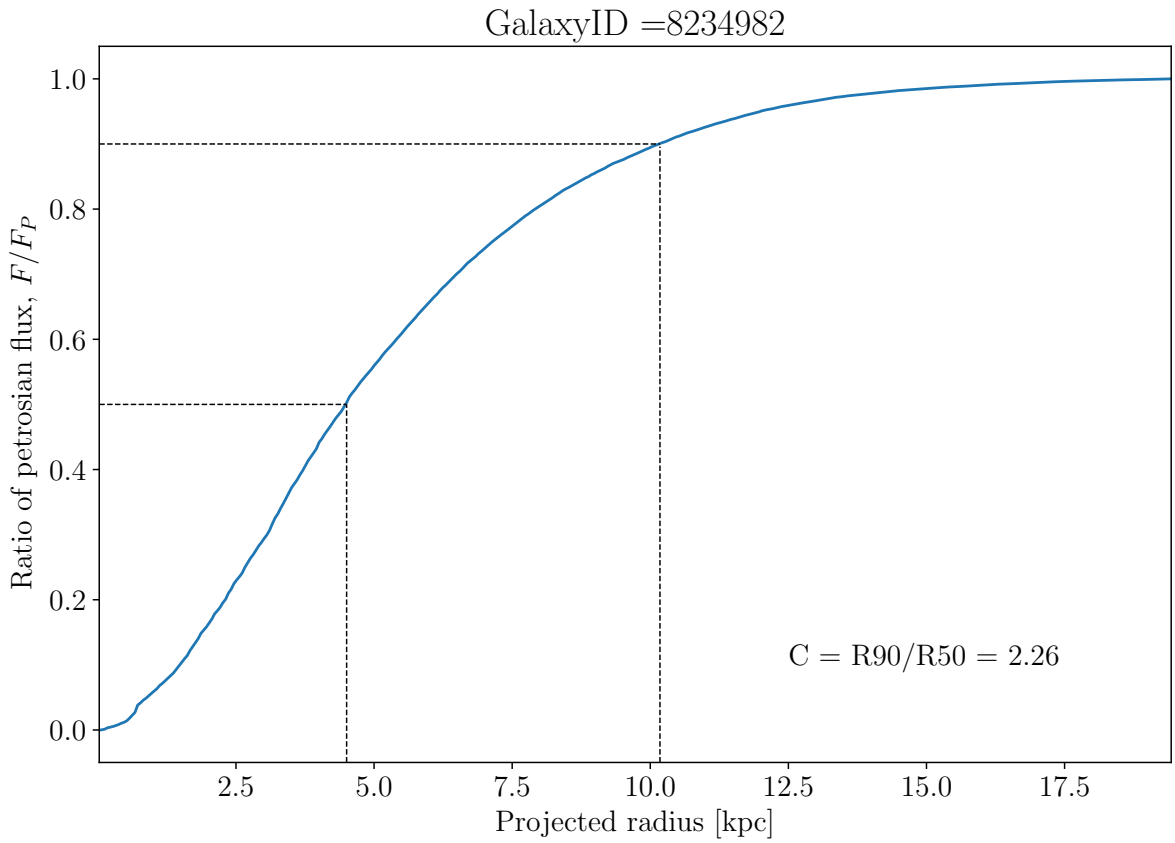

Figure 3.5: Ratio of the Petrosian flux for the galaxy 8234982 along the projected radius. The dashed lines show the value of the radius that contains the 50% (R50) and the 90% (R90) of the Petrosian flux.

3.4 Formation history and merger relations

At this point, we have decomposed the stellar particles in disk, halo, and bulge, and also we have obtained the light concentration index. We are now in a position to study the evolution of these galaxies and to check whether there is a dependence with the size of their bulge.

To do this, it is necessary to take into account the formation history of each galaxy. EAGLE database stores, for each of its galaxies, the information of its last progenitor and its descendant. With this, and taking into account that our sample has been chosen at z=0, it is possible to recreate the complete formation history. An example is shown at figure 3.6.

Once the formation history is obtained, it is possible to perform an analysis of the mergers that have taken place. In this case we will only consider mergers with a redshift lower than z = 3 to avoid the early accretion events. We select the accreted satellite galaxy that had the most impact on the final mass of the galaxy via merger. For each

snapshot, we compute the mass ratio between the satellite galaxies that are going to be merged during the next step with their final galaxy.

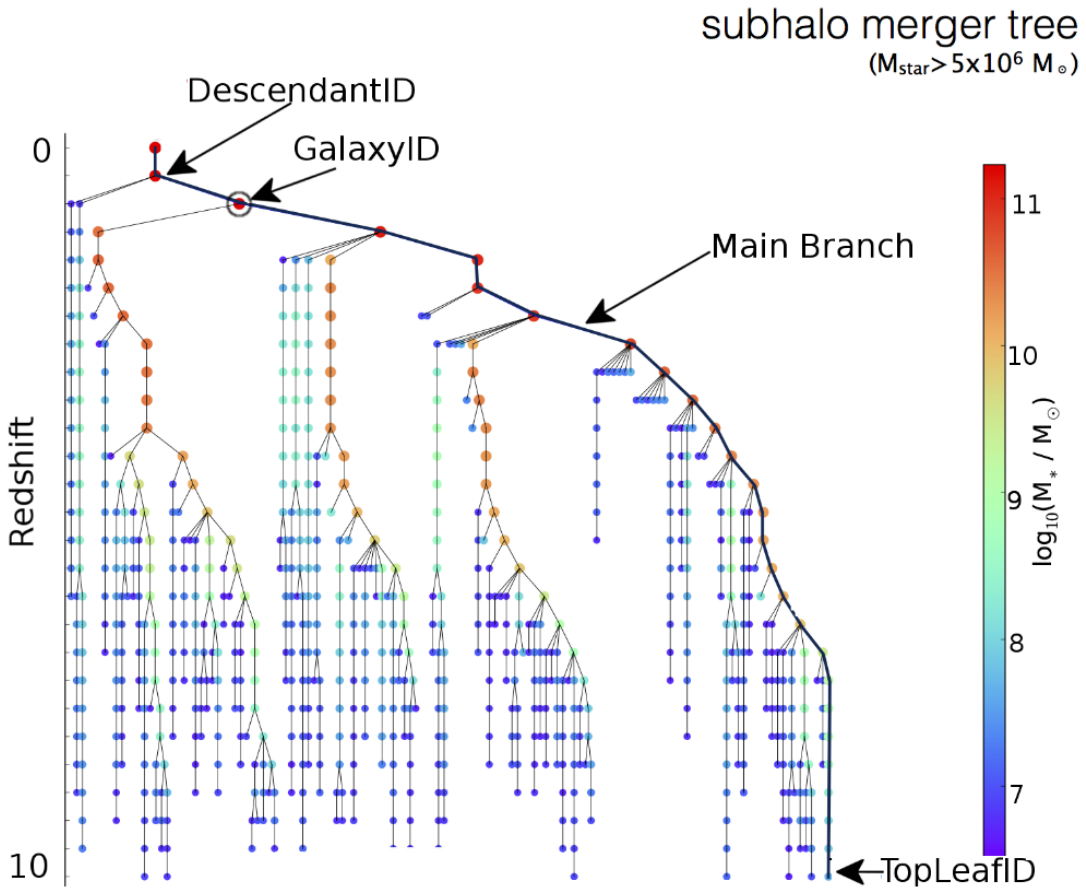

Figure 3.6: Merger history of a galaxy with a z = 0.18 stellar mass $M_* \sim 10^{10} M_\odot$ indicated by the circled dot. Symbol colours and sizes are scaled with the logarithm of the stellar mass. The GalaxyID of this galaxy points towards it, as indicated by the arrow. The main progenitor branch is indicated with a thick black line, all other branches with a thin line. The TopLeafID gives the GalaxyID of the highest redshift galaxy on the main progenitor branch whilst the LastProgID (not shown) gives the maximum GalaxyID of all the progenitors of the galaxy considered. Querying all galaxies with an ID between GalaxyID and LastProgID will return all the progenitor galaxies in the tree. Figure extracted from McAlpine et al. (2016).

In section 4.2 we will see the result of this study and its dependency with their kinematics and photometric parameters. We also study the mean age of the stellar particles belonging to the spheroidal and bulge components and their possible dependence on the component size. We perform this analysis only for the Zolotov et al. (2009) decomposition, since it is the only technique that provides us with information on the stellar particles of each component.

Chapter 4

Results

In this chapter, the results obtained with the methods introduced in section 3.3 will be laid out. A brief analysis of the galaxy kinematic decomposition and the photometric classification will be carried out in sections 4.1.1 and 4.1.2, respectively. An analysis of the correlation between the size of the bulge and their galaxy's formation history will be shown in 4.2.

4.1 Preliminary classifications

In the following sections, we are going to exhibit the results for the three different decomposition techniques used in this work. Section 4.1.1 is dedicated to the kinematic analysis (Zolotov et al., 2009; Clauwens et al., 2018) that we applied for the largest simulation of EAGLE (Crain et al., 2015; Schaye et al., 2015), their similarities and differences. Later, in section 4.1.2, we will set a kinematic threshold for bulgeless galaxies through the photometric cut (Graham & Driver, 2005). The fraction of bulgeless galaxies in the sample is calculated for each of the techniques used (table 4.1).

4.1.1 Kinematic decomposition

In this section, we aim to estimate the mass contribution of the different components for the simulated massive disk galaxies of the sample (section 3.2) in the two methods used.

Figures 4.1 and 4.2 present the results of the decomposition following Zolotov et al. (2009) and Clauwens et al. (2018), as discussed in section 3.3.1. Both figures show the evolution of disk, spheroidal, bulge and halo mass components for central Milky Way-like galaxies, shown in red, black, cyan and green lines, respectively. The black line indicates the spheroidal component, S, while the dashed black line indicates the stars within the component 1-S, which, by construction, includes also the disk. We have indicated the 10th and 90th percentiles, only for the main components.

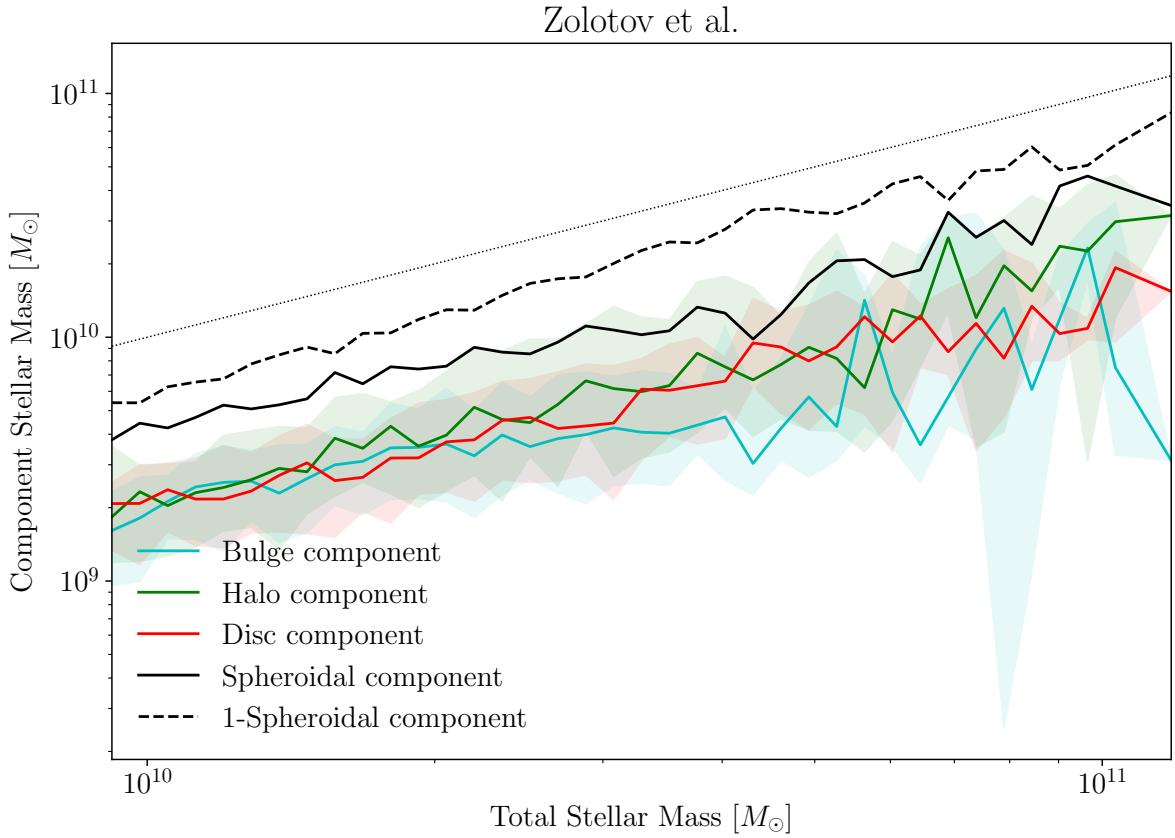

Figure 4.1: Stellar mass component of the galaxies for the main progenitors of central galaxies measured by the Zolotov et al. (2009) method. The dark lines represent the spheroidal (solid black line) and the non-spheroidal mass component (dashed black line). The stellar bulge and halo components, belonging to the spheroidal one, are represented in cyan and green, respectively. The red line shows the disk component, belonging to the non-spheroidal component. All the curves represent running medians and we have indicated their 10th and 90th percentiles only for the disk, bulge and halo mass components. The total mass is indicated by a dotted black line.

One can quantify the relative importance of the components using the two different methods. If we take a brief view on figure 4.1, we can see how, although we selected a sample with 'disky' galaxies, the mass of the disk component is consistently smaller than the spheroidal one. Indeed, only around 30% of the non-spheroidal stellar mass belong to the disk component. The j_z/j_c cut that Zolotov et al. (2009) defines, described above, leaves a set of stars whose kinematics do not meet neither the disk nor the spheroid criteria. These stars could belong to rotational components such as the thick disk and the pseudo-bulge. This result differs with figure 4.2, where the disk component is comparable with the stellar particles that do not belong to the spheroidal component, both always larger than the bulge component. Moreover, despite the fact that Clauwens et al. (2018) also use a criteria for identifying the disk, they do not consider the existence of other rotational components like pseudo-bulges or bars, and apply a simpler decomposition. Of

course, galaxies have more complicated structure than just a disk and a spheroid, but both decompositions are useful to extract the bulge component.

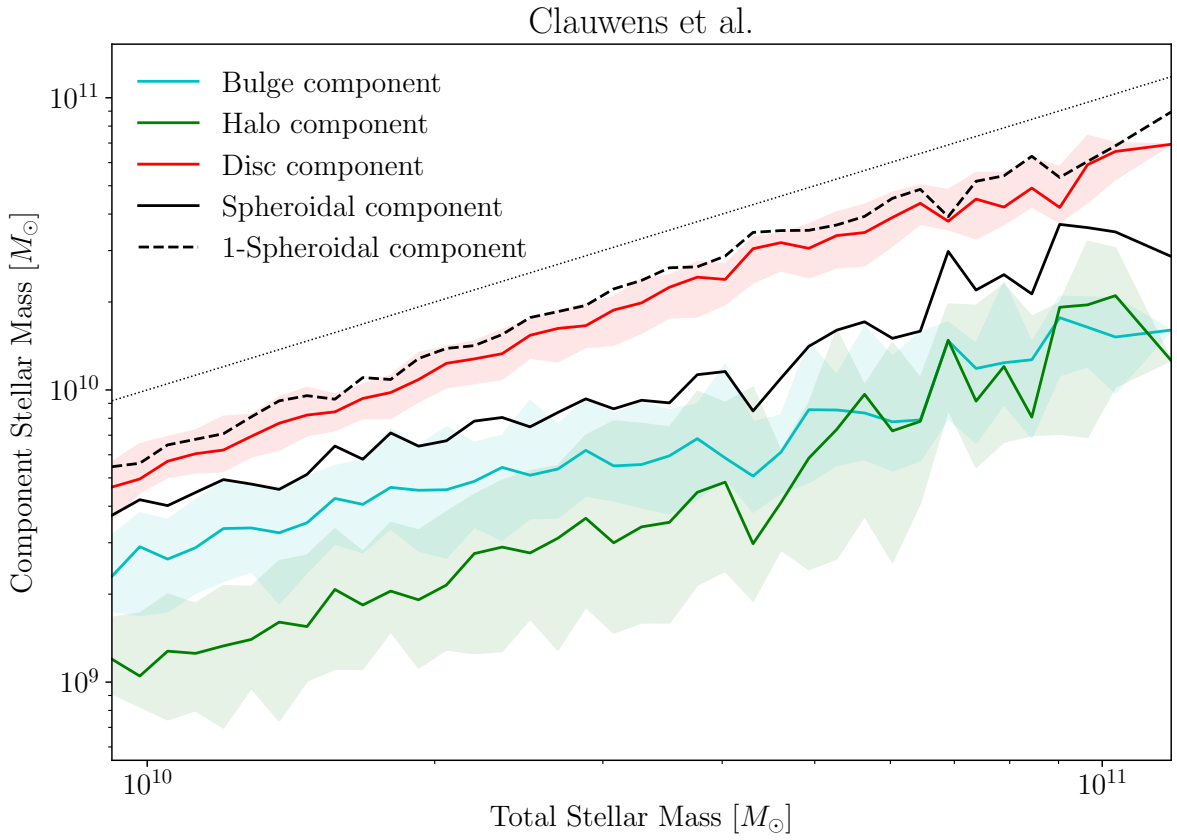

Figure 4.2: Same diagnostic as in figure 4.1 for the Clauwens et al. (2018) method. The dark lines represent the spheroidal (solid black line) and the non-spheroidal mass component (dashed black line). The stellar bulge and halo components, belonging to the spheroidal one, are represented in cyan and green, respectively. The red line shows the disk component, belonging to the non-spheroidal component. All the curves represent running medians and we have indicated their 10th and 90th percentiles only for the disk, bulge and halo mass components. The total mass is indicated by a dotted black line.

Aiming to further compare the two methods, figure 4.3 shows the spheroidal and bulge components for each one. Hereafter, results obtained using Clauwens et al. (2018) technique will be represented by dashed lines, whereas the solid lines will denote Zolotov et al. (2009) method. The 10th and 90th percentiles are also shown in each figure. The black lines are referred to the spheroidal component in each case with the aim to have a better comparison. Even though there is an obvious distinction between kinematic methods when referring to the disk component, figure 4.3 indicates that there is no such difference between the masses of the spheroidal component. Also, although the definition of the bulge is quite different in the two methods, the masses of the bulge are also similar.

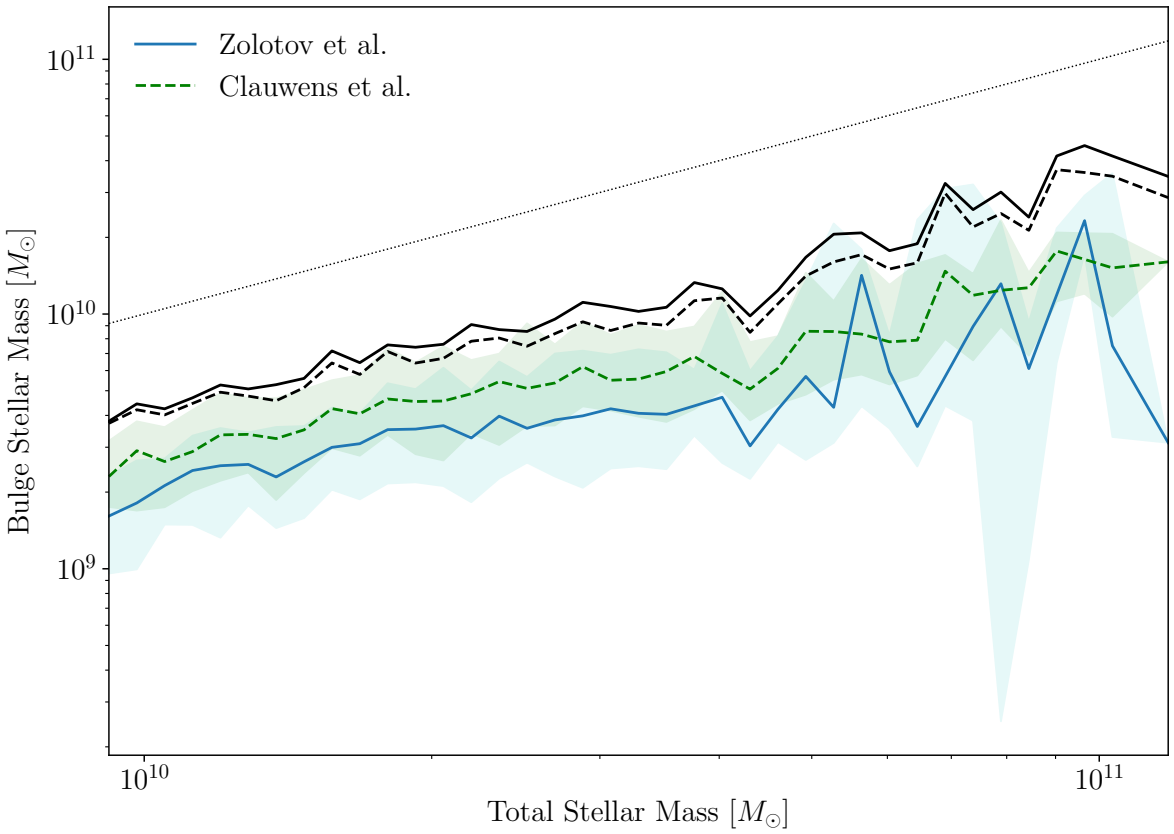

Figure 4.3: Bulge mass component of central galaxies measured by the two methods used. The dark lines represent the spheroidal component in both methods. The components corresponding to the Zolotov et al. (2009) decomposition are shown with solid lines whereas the Clauwens et al. (2018) components are drawn with dashed lines. All the curves represent running medians and we have indicated their 10th and 90th percentiles only for the stellar bulge component. The total mass is indicated by a dotted black line.

4.1.2 Photometric decomposition

In this section, knowing the concentration index threshold of 2.5 for determining bulgeless galaxies (section 1.2.1), we are going to look for the corresponding kinematic threshold. We found that about 24% of the galaxies in the sample have a light concentration lower than this value, which agrees with Barazza et al. (2008). Within this attempt, we determine the dependence of S/T and B/T on the light concentration index.

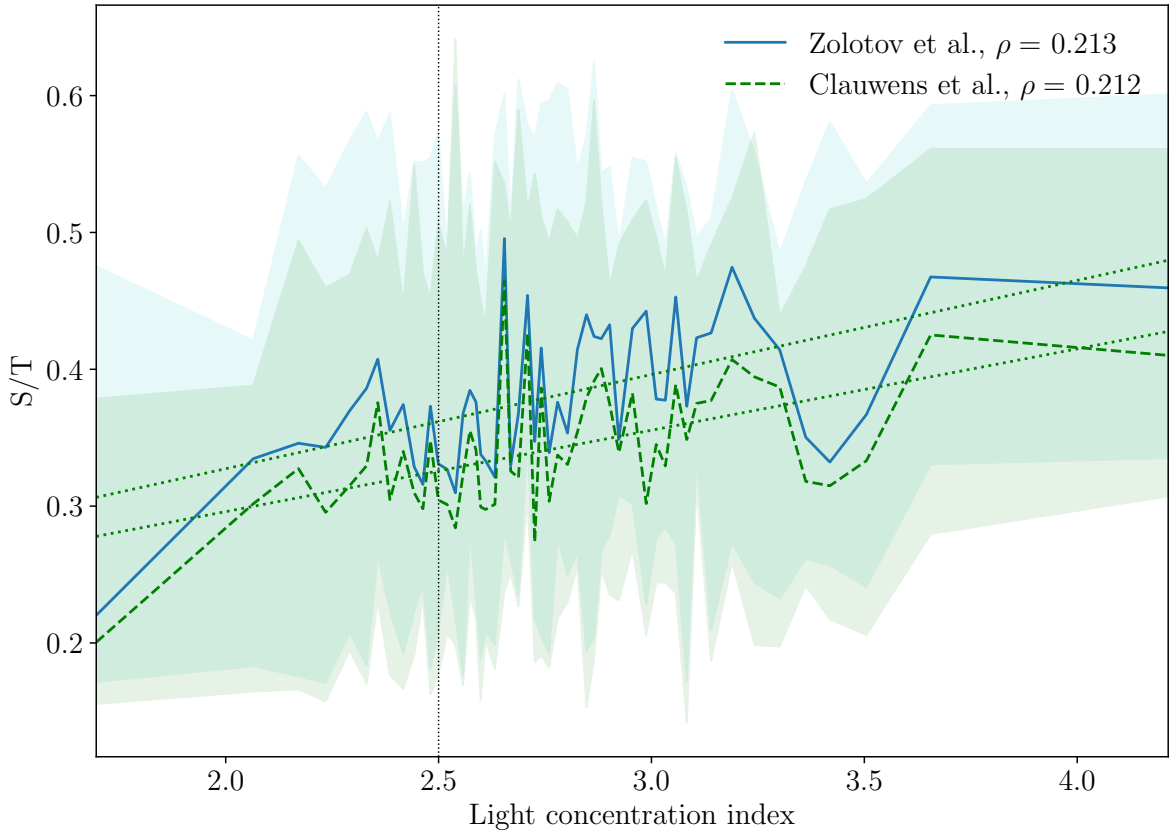

Figure 4.4: The spheroidal-to-total stellar mass ratio as a function of the light concentration index of central galaxies measured by the two methods used. The component corresponding to the Zolotov et al. (2009) decomposition is shown with a blue solid line whereas the Clauwens et al. (2018) component is drawn with a green dashed line. The curves represent running medians and we have indicated their 10th and 90th percentiles. The dotted lines represent the linear fit of the medians for each method. The vertical line shows the threshold used by the BEARD project (section 1.2.1) to select their bulgeless sample. For each curve, the Pearson correlation coefficient, ρ, is also shown in the respective legend.

Figures 4.4 and 4.5 show the correlation of the light concentration index with the spheroidal and bulge components, respectively. The 10th and 90th percentiles are also shown for each case. The Pearson correlation coefficient, ρ, are also shown in the legend for both methods. Now, we are able to find the kinematic cut that corresponds to a concentration of 2.5. In table 4.1 we can see this cut and the kinematic fraction of non spheroidal and bulgeless galaxies found for each method. One needs to take into account that the correlation values of $\rho \sim 0.2$ may not be significant enough to make a proper selection of bulgeless galaxies. In fact, figures 4.4 and 4.5 show how, for Zolotov et al. (2009) method, the spheroidal component shows a stronger correlation with the concentration parameter than the bulge component.

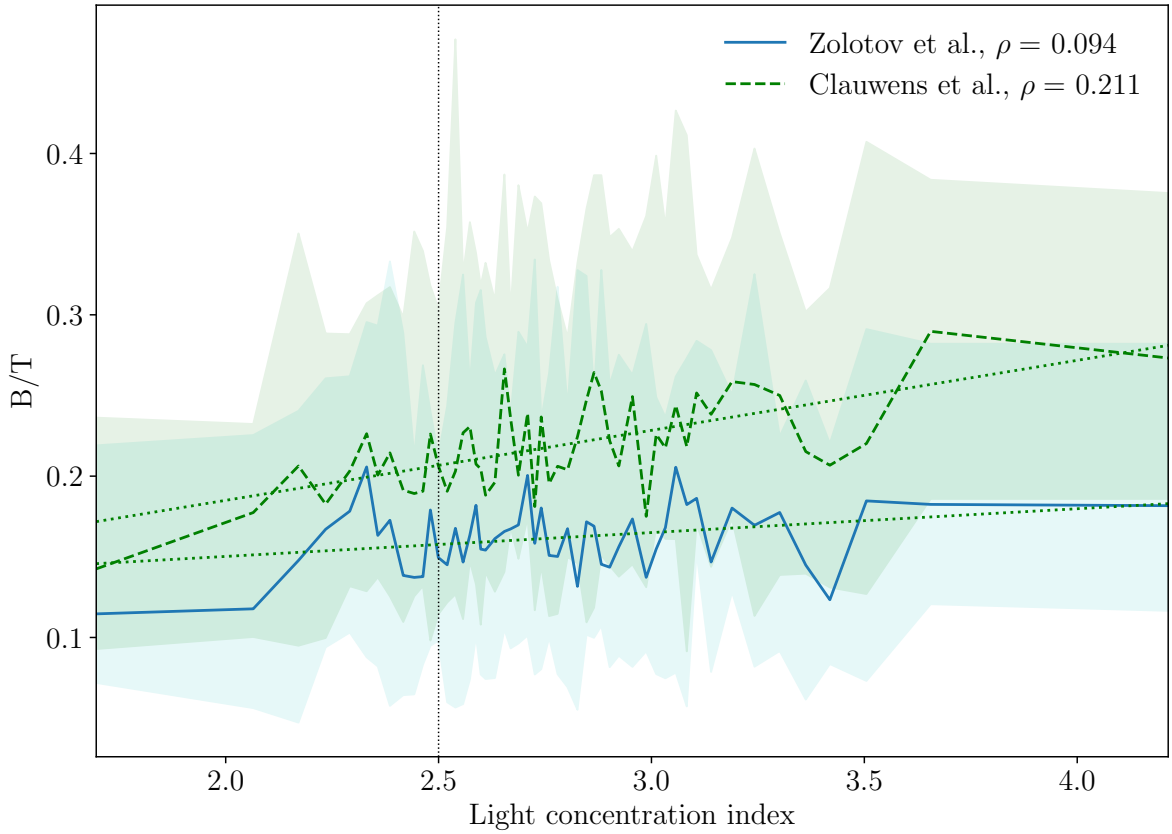

Figure 4.5: The same diagnostic as in figure 4.4 but using the bulge-to-total stellar mass ratio as a function of the light concentration index. The component corresponding to the Zolotov et al. (2009) decomposition is shown with a blue solid lines whereas the Clauwens et al. (2018) component is drawn with a green dashed line. The curves represent running medians and we have indicated their 10th and 90th percentiles. The dotted lines represent the linear fit of the medians for each method. The vertical line shown the threshold used by the BEARD project (section 1.2.1) to select their bulgeless sample. The Pearson correlation coefficient, ρ, is also shown for each curve in the legend.

The derived thresholds for bulgeless galaxies and the percent of bulgeless galaxies identified by the two kinematic methods can be found in table 4.1. We find that about 50% of the galaxies of our sample can be classified as bulgeless galaxies using the kinematic thresholds. This percentage is substantially higher, around a factor of two, than that from photometry. However, it is still within the ranges that Barazza et al. (2008) and Kormendy et al. (2010) established in their studies (section 1.2).

	S/T_{cut}	$S/T < S/T_{cut}$	B/T_{cut}	$B/T < B/T_{cut}$
Zolotov et al. (2009)	0.36	43.85%	0.16	48.88%
Clauwens et al. (2018)	0.33	57.09%	0.21	46.76%

Table 4.1: Threshold and percent of non-spheroidal and bulgeless galaxies measured for our sample with each technique used.

4.2 Formation history and major mergers relations

As discussed in section 1.2, mergers are thought to play a major role in bulge growth and morphological changes. For this reason, we are going to study the contribution of accreted satellite galaxies to their final stellar mass, throughout the galaxy formation history. To do so, we extract from the formation history the largest satellite that merged with the galaxy and measure the mass contribution to the final galaxy. This provides us a view of the largest mass change that the final galaxies had during their formation.

Figures 4.6 and 4.7 show the correlation between the largest stellar mass accretion in the formation history and the S/T and B/T ratio, respectively. In addition, we also analyse the correlation with the light concentration parameter in figure 4.8. For each figure, we represent running medians and their 10th and 90th percentiles. A measure of the Pearson correlation coefficient, ρ, is also shown. One can see how the kinematic components (figures 4.6 and 4.7) have a Pearson correlation coefficient less than 0.1. Therefore, we do not have a significant correlation value to make any proper conclusion.

Although the correlation coefficient of figure 4.8 is also low, one can appreciate a slight dependence with the largest mass accretion. Galaxies with stronger light concentration have had a larger mass contribution via merger. Likewise, galaxies that can be catalogued as bulgeless galaxies show that the contribution of mass via merger has been lower.

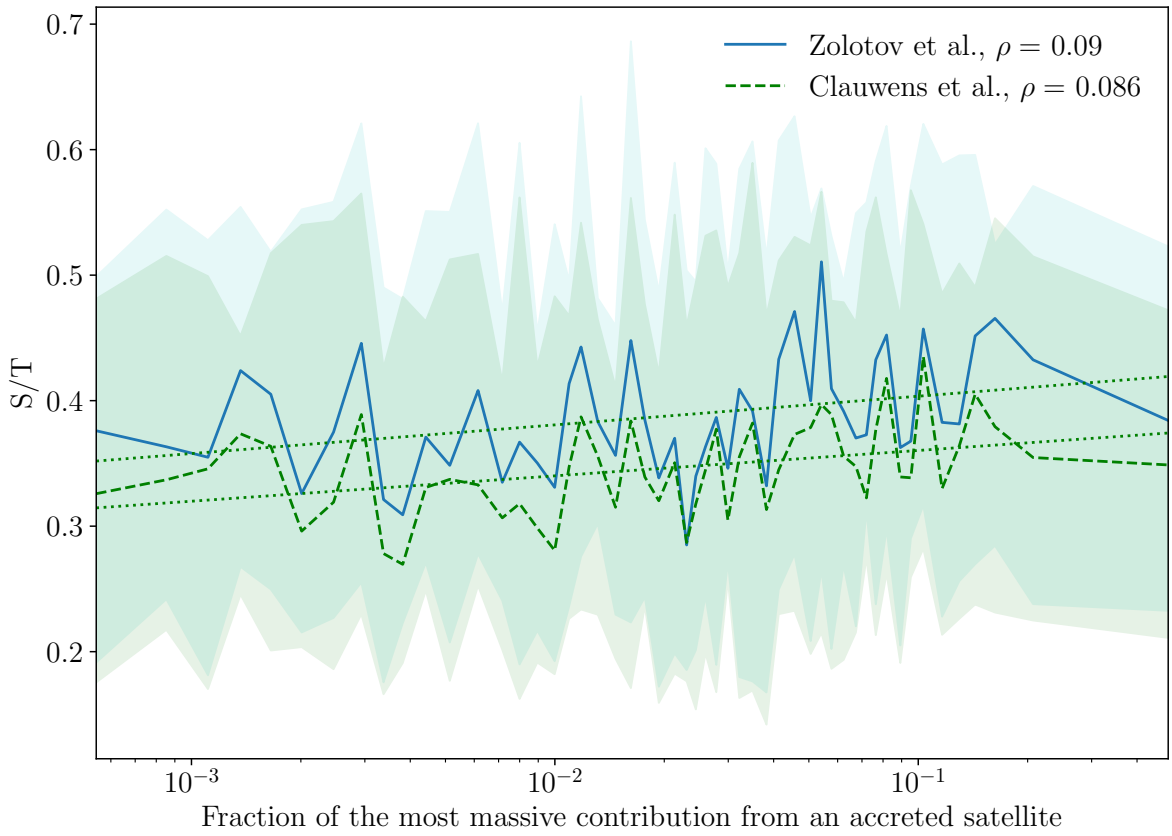

Figure 4.6: Dependence of the spheroidal-to-total stellar mass ratio as a function of the most massive contribution from an accreted satellite. The component corresponding to the Zolotov et al. (2009) decomposition is shown with a blue solid line whereas the Clauwens et al. (2018) component is drawn with a green dashed line. The curves represent running medians and we have indicated their 10th and 90th percentiles. The dotted lines represent the linear fit of the medians for each method. The Pearson correlation coefficient, ρ, is also shown for each curve in the legend.

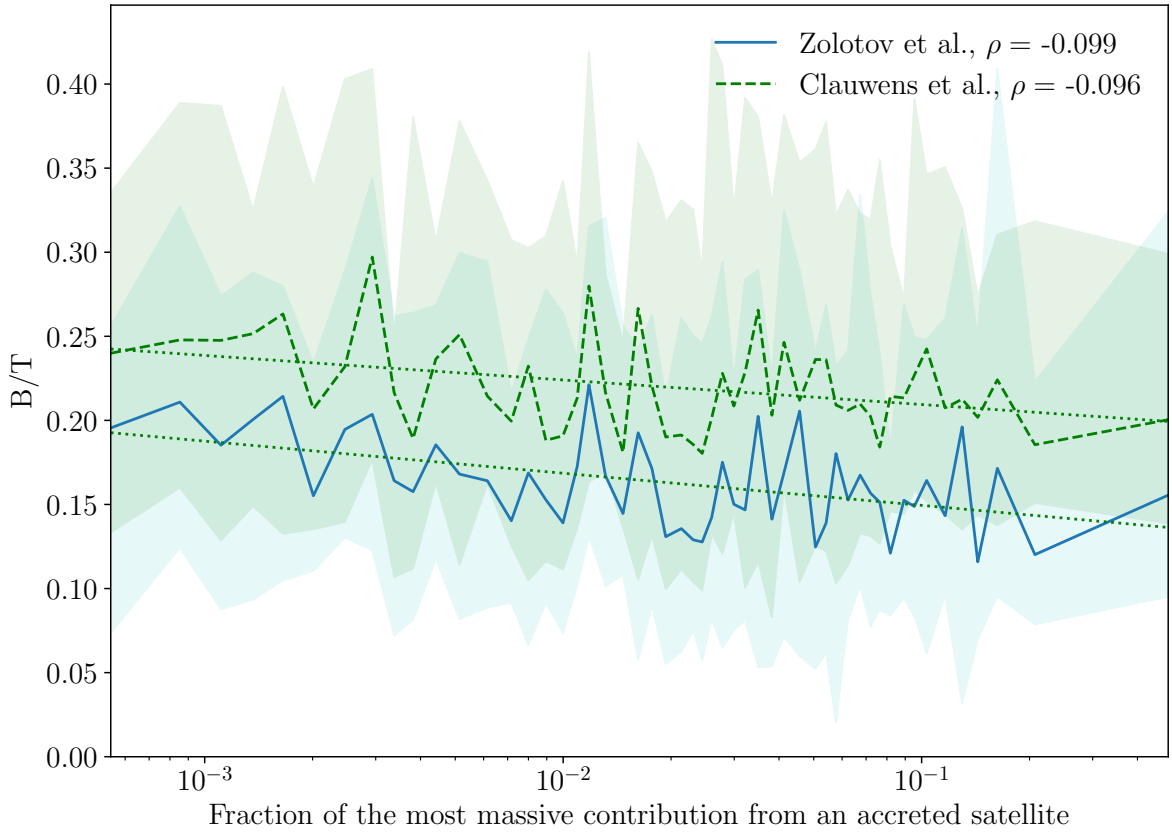

Figure 4.7: Dependence of the bulge-to-total stellar mass ratio as a function of the most massive contribution from an accreted satellite. The component corresponding to the Zolotov et al. (2009) decomposition is shown with a blue solid line whereas the Clauwens et al. (2018) component is drawn with a green dashed line. The curves represent running medians and we have indicated their 10th and 90th percentiles. The dotted lines represent the linear fit of the medians for each method. The Pearson correlation coefficient, ρ, is also shown for each curve in the legend.

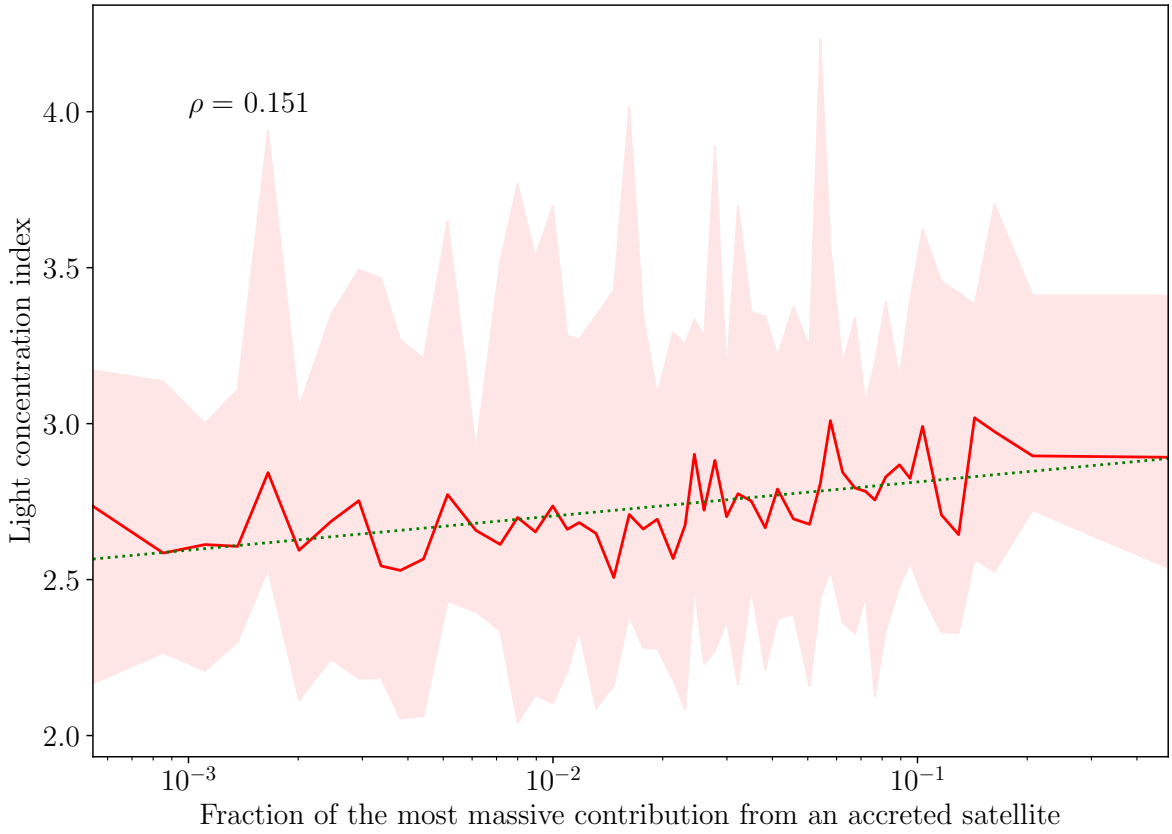

Figure 4.8: Dependence of the light concentration index as a function of the most massive contribution from an accreted satellite, shown in red. The curve represents running median and we have indicated its 10th and 90th percentiles. The dotted lines represent the linear fit of the curve. The Pearson correlation coeficient, ρ, is also shown.

Zolotov et al. (2009) method provides us with the particles belonging to each component. With this information, we can study the average age of the stellar particles that belong to the spheroidal and bulge components and study if there is any correlation with the size of their correspondent component, this is shown in figure 4.9. One can appreciate the sharp difference between the correlation coefficient for both component. The stellar bulge component has a correlation value, ρ, close to 0 that indicates no correlation. On the other hand, we can appreciate a slight correlation for the spheroidal component. Those galaxies with smaller spheroidal component have an older stellar population, with a stellar average age corresponding to a redshift $z < 3$. Whereas galaxies with a massive spheroidal component have a stellar average age of $z \sim 1$. The presence of the correlation only for the spheroidal component and not for the stellar bulge indicates the existence of the correlation in the stellar halo. If this small correlation is to be trusted, the result is in agreement with a merger scenario, in which a significant fraction of stellar particles belonging to the halo were formed ex-situ.

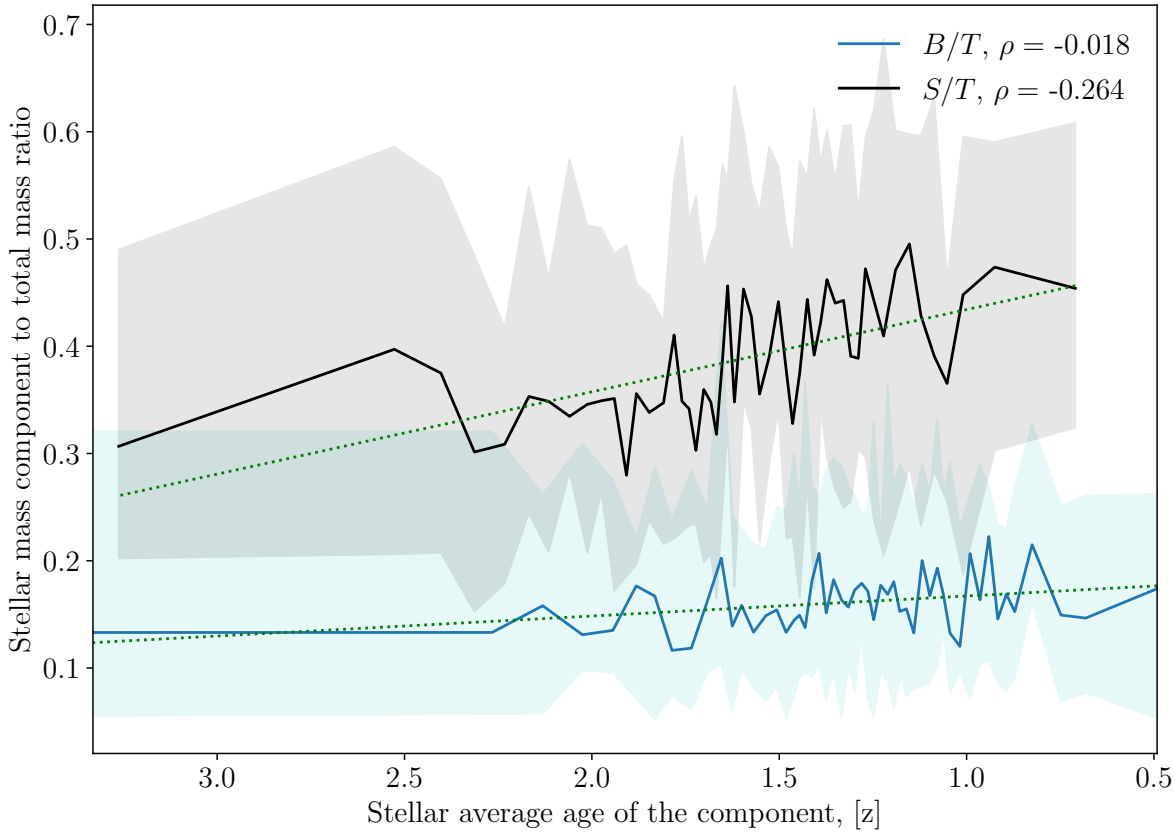

Figure 4.9: Dependence of spheroidal-to-total mass ratio and bulge-to-total mass ratio with the stellar average age of the component. The curves show running medians with their 10th and 90th percentiles. The line corresponding to the spheroidal component is shown in black and the bulge component is shown in blue. Both curves have a linear fit shown with a dotted line. The Pearson correlation coefficient, ρ, is also shown for each curve in the legend.

Throughout this chapter, we have seen how the correlation coefficient for each result is too low to provide conclusive statements. We know that the minimum resolved scale in this simulation is about 1 kpc. However, even though we are working within the range of massive galaxies, higher resolution is needed to confidently resolve bulgeless galaxies. Furthermore, in order to decrease the error in the statistics, larger simulations are needed.

Chapter 5

Conclusions

In the framework of this *Trabajo de Fin de Máster*, we have used state-of-the-art kinematic decompositions and observational techniques with the larger simulation of EAGLE, designed for simulating the evolution of individual galaxies with high resolution and in a cosmological volume. In order to do this, we had to understand the underlying mathematical structure of the diverse decomposition techniques used.

We used two kinematic techniques (Zolotov et al., 2009; Clauwens et al., 2018), both based on the angular momenta of the stellar particles to separate each galaxy into a spheroidal and disk component. In addition, we separate the spheroidal component into a stellar bulge and stellar halo (section 3.3.1). Also, in order to make a direct comparison with the BEARD observations, we also make a photometric decomposition, based on Graham & Driver (2005) (section 3.3.2), which allow us to identify the bulgeless galaxies in our sample, i.e., those that have a light concentration lower than a value of 2.5. We found that about 24% of our sample have a light concentration lower than this value. With this photometric threshold, we make a direct comparison with the kinematics decomposition to establish an analogue cut. The bulgeless threshold and the percent of galaxies within that cut are found for each method and are shown in table 4.1. We find that about 50% of the galaxies of our sample can be catalogued as bulgeless galaxies within the kinematic threshold. Both conclusions are within the range that Barazza et al. (2008) and Kormendy et al. (2010) provide in their studies.

With the previously acquired knowledge, we made an analysis on the formation history of Milky Way-like galaxies and their relation in the size of their spheroid and stellar bulge components (Fig. 4.6, 4.7). In addition, we also studied the correlation between the light concentration index and their formation history, figure 4.8.

Finally, taking advantage of the fact that the Zolotov et al. (2009) technique gives us information about the particles belonging to each component, a study of the average stellar age of the spheroidal and stellar bulge was made in figure 4.9. A slight dependence with the average age and the size of their component can be seen only for the spheroidal component.

5.1 Future Work

Although a slight dependence of the kinematic and photometric parameters and their formation history can be found in this work, this results are clearly not enough to make any strong affirmation. For this reason, different studies can be performed in the future. We can summarize the short term goal in:

1. Make a deeper study of the bulge evolution of our sample. To do this, it is needed an analysis of the whole bulge evolution throughout the formation history and their mass growth.

2. Compare the theoretical B/T parameter with the SSDS observational B/T using the BEARD project sample to identify the fraction of bulgeless galaxies more accurately.

3. Study the origin of the stellar particles belonging to the bulge and the correlation with the amount of stellar particles that initially belong to another galaxy and the size of the bulge component.

4. Use higher-resolution cosmological simulations as COLIBRI or ILUSTRIS-TNG to increase the resolution of our study.

If all the preceding goals are achieved, the result could be a challenge to current hierarchical models and play a crucial role to understand both the merger history of bulgeless galaxies and their evolutionary path.

Chapter 6

Bibliography

Ade, P. A. R., Aghanim, N., Alves, M. I. R., et al. 2014, Astronomy Astrophysics, 571, A1

Aguerri, J. A. L., Balcells, M., & Peletier, R. F. 2001, Astronomy Astrophysics, 367

Andredakis, Y. C. & Sanders, R. H. 1994, Monthly Notices of the Royal Astronomical Society, 267

Aumer, M., White, S. D. M., & Naab, T. 2014, Monthly Notices of the Royal Astronomical Society, 441

Aumer, M., White, S. D. M., Naab, T., & Scannapieco, C. 2013, Monthly Notices of the Royal Astronomical Society, 434

Barazza, F. D., Jogee, S., & Marinova, I. 2008, The Astrophysical Journal, 675

Blanton, M. R., Dalcanton, J., Eisenstein, D., et al. 2001, The Astronomical Journal, 121

Bluck, A. F. L., Mendel, J. T., Ellison, S. L., et al. 2014, Monthly Notices of the Royal Astronomical Society, 441

Bottrell, C., Torrey, P., Simard, L., & Ellison, S. L. 2017, Monthly Notices of the Royal Astronomical Society, 467

Bournaud, F., Chapon, D., Teyssier, R., et al. 2011, The Astrophysical Journal, 730

Bournaud, F., Elmegreen, B. G., & Elmegreen, D. M. 2007, The Astrophysical Journal, 670

Brook, C. B., Governato, F., Roškar, R., et al. 2011, Monthly Notices of the Royal Astronomical Society, 415

Brooks, A. & Christensen, C. 2016, Bulge Formation via Mergers in Cosmological Simulations

Böker, T., Laine, S., van der Marel, R. P., et al. 2002, The Astronomical Journal, 123

Cappellari, M., Emsellem, E., Krajnović, D., et al. 2011, Monthly Notices of the Royal Astronomical Society, 416

Ceverino, D., Dekel, A., Tweed, D., & Primack, J. 2015, Monthly Notices of the Royal Astronomical Society, 447

Christensen, C. R., Brooks, A. M., Fisher, D. B., et al. 2014, Monthly Notices of the Royal Astronomical Society: Letters, 440

Clauwens, B., Schaye, J., Franx, M., & Bower, R. G. 2018, Monthly Notices of the Royal Astronomical Society, 478

Correa, C. A., Schaye, J., Clauwens, B., et al. 2017

Crain, R. A., McCarthy, I. G., Frenk, C. S., Theuns, T., & Schaye, J. 2010, Monthly Notices of the Royal Astronomical Society, 407

Crain, R. A., Schaye, J., Bower, R. G., et al. 2015, Monthly Notices of the Royal Astronomical Society, 450, 1937

Croft, R. A. C., Weinberg, D. H., Katz, N., & Hernquist, L. 1998, The Astrophysical Journal, 495, 44

Djorgovski, S. & Spinrad, H. 1981, The Astrophysical Journal, 251

Eggen, O. J., Lynden-Bell, D., & Sandage, A. R. 1962, The Astrophysical Journal, 136

Fisher, D. B. & Drory, N. 2011, The Astrophysical Journal, 733

Gadotti, D. A. 2009, Monthly Notices of the Royal Astronomical Society, 393

Governato, F., Brook, C., Mayer, L., et al. 2010, Nature, 463

Governato, F., Brook, C. B., Brooks, A. M., et al. 2009, Monthly Notices of the Royal Astronomical Society, 398

Graham, A. W. & Driver, S. P. 2005, Publications of the Astronomical Society of Australia, 22

Guedes, J., Mayer, L., Carollo, M., & Madau, P. 2013, The Astrophysical Journal, 772

Hernquist, L. 1989, Nature, 340

Hopkins, P. F., Bundy, K., Croton, D., et al. 2010, The Astrophysical Journal, 715

Hubble, E. P. 1936, Realm of the Nebulae

Jenkins, A. 2010, Monthly Notices of the Royal Astronomical Society, 403, 1859

Karachentsev, I. 1989, The Astronomical Journal, 97

Karachentsev, I. D. 1999, Astronomy Letters, 25, 318

Karachentsev, I. D., Karachentseva, V. E., & Parnovsky, S. L. 1993, Astronomische Nachrichten: A Journal on all Fields of Astronomy, 314

Kautsch, S. J. 2009, Publications of the Astronomical Society of the Pacific, 121

Kormendy, J. & Bender, R. 2012, The Astrophysical Journal Supplement Series, 198

Kormendy, J., Drory, N., Bender, R., & Cornell, M. E. 2010, The Astrophysical Journal, 723

Kormendy, J. & Kennicutt, R. C. 2004, Annual Review of Astronomy and Astrophysics, 42

Krumholz, M. R., Burkhart, B., Forbes, J. C., & Crocker, R. M. 2018, Monthly Notices of the Royal Astronomical Society, 477

Lucia, G. D., Fontanot, F., Wilman, D., & Monaco, P. 2011, Monthly Notices of the Royal Astronomical Society, 414

McAlpine, S., Helly, J. C., Schaller, M., et al. 2016, Astronomy and Computing, 15, 72

McCarthy, I. G., Font, A. S., Crain, R. A., et al. 2012, Monthly Notices of the Royal Astronomical Society, 420

McDonald, P., Seljak, U., Cen, R., et al. 2005, The Astrophysical Journal, 635, 761

Mitronova, S. N., Karachentsev, I. D., Karachentseva, V. E., Jarrett, T. H., & Kudrya, Y. N. 2004, Bulletin of the Special Astrophysics Observatory, 57, 5

Méndez-Abreu, J., Ruiz-Lara, T., Sánchez-Menguiano, L., et al. 2017, Astronomy Astrophysics, 598

Navarro, J. F., Ludlow, A., Springel, V., et al. 2010, Monthly Notices of the Royal Astronomical Society, 402

Noguchi, M. 1999, The Astrophysical Journal, 514

Nordström, B., Mayor, M., Andersen, J., et al. 2004, Astronomy Astrophysics, 418

Perez, J., Valenzuela, O., Tissera, P. B., & Michel-Dansac, L. 2013, Monthly Notices of the Royal Astronomical Society, 436

Pohlen, M., Balcells, M., Lütticke, R., & Dettmar, R.-J. 2003, Astronomy Astrophysics, 409

Power, C., Navarro, J. F., Jenkins, A., et al. 2003, Monthly Notices of the Royal Astronomical Society, 338

Raha, N., Sellwood, J. A., James, R. A., & Kahn, F. D. 1991, Nature, 352

Sales, L. V., Navarro, J. F., Schaye, J., et al. 2010, Monthly Notices of the Royal Astronomical Society, 409, 1541

Sales, L. V., Navarro, J. F., Theuns, T., et al. 2012, Monthly Notices of the Royal Astronomical Society, 423

Sandage, A. & Perelmuter, J.-M. 1990, The Astrophysical Journal, 350

Scannapieco, C., Gadotti, D. A., Jonsson, P., & White, S. D. M. 2010, Monthly Notices of the Royal Astronomical Society: Letters, 407

Schaye, J., Crain, R. A., Bower, R. G., et al. 2015, Monthly Notices of the Royal Astronomical Society, 446, 521

Schaye, J., Theuns, T., Rauch, M., Efstathiou, G., & Sargent, W. L. 2000, Monthly Notices of the Royal Astronomical Society, 318, 817

Shen, J., Rich, R. M., Kormendy, J., et al. 2010, The Astrophysical Journal, 720

Sparre, M. & Springel, V. 2017, Monthly Notices of the Royal Astronomical Society, 470

Springel, V. 2005, Monthly Notices of the Royal Astronomical Society, 364

Tacchella, S., Carollo, C. M., Renzini, A., et al. 2015, Science, 348

Thob, A. C., Crain, R. A., McCarthy, I. G., et al. 2019, Monthly Notices of the Royal Astronomical Society, 485, 972

van Dokkum, P. G., Bezanson, R., van der Wel, A., et al. 2014, The Astrophysical Journal, 791

Viel, M., Haehnelt, M. G., & Springel, V. 2004, Monthly Notices of the Royal Astronomical Society, 354, 684

Whitaker, K. E., Franx, M., Bezanson, R., et al. 2015, The Astrophysical Journal, 811

White, S. D. M. & Rees, M. J. 1978, Monthly Notices of the Royal Astronomical Society, 183

Wyse, R. F. G., Gilmore, G., & Franx, M. 1997, Annual Review of Astronomy and Astrophysics, 35

Zavala, J., Frenk, C. S., Bower, R., et al. 2016, Monthly Notices of the Royal Astronomical Society, 460

Zjupa, J. & Springel, V. 2017, Monthly Notices of the Royal Astronomical Society, 466

Zolotov, A., Willman, B., Brooks, A. M., et al. 2009, The Astrophysical Journal, 702